

REVERBERANT ELECTROMAGNETIC FIELDS
WITHIN LAUNCH VEHICLE
PAYLOAD FAIRINGS

By

SHABIR KABIRI

Bachelor of Science in Electrical Engineering

The United States Military Academy

West Point, New York

2016

Submitted to the Faculty of the
Graduate College of the
Oklahoma State University
in partial fulfillment of
the requirements for
the Degree of
MASTER OF SCIENCE
July 2020

REVERBERANT ELECTROMAGNETIC FIELDS
WITHIN LAUNCH VEHICLE
PAYLOAD FAIRINGS

Thesis Approved:

Dr. Jim West

Thesis Adviser

Dr. Chuck Bunting

Dr. John O'Hara

ACKNOWLEDGEMENTS

I acknowledge my parents and siblings for their unconditional love and faith in me. I acknowledge my thesis advisor, Dr. Jim West for his mentoring, and guidance during my thesis work. Dr. Chuck Bunting encouraged me to maintain high work standards, and be adventurous in exploring research topics. I acknowledge Mehdi Bahadorzadeh, post-doc at OSU ECE, for going above and beyond to help me in setting up the tests for this thesis.

Sincere thanks go to OSU MAE for fabricating the payload fairing scale model and I would like to acknowledge NASA and Robust Physics for supporting this study.

Name: SHABIR KABIRI

Date of Degree: JULY 2020

Title of Study: REVERBERANT ELECTROMAGNETIC FIELDS WITHIN LAUNCH
VEHICLE PAYLOAD FAIRINGS

Major Field: ELECTRICAL ENGINEERING

Abstract: A launch vehicle payload fairing scale model has been designed, fabricated, and tested at Oklahoma State University to investigate the reverberant electromagnetic fields within launch vehicle fairings. The OSU fairing model uses a mechanical stirrer to attain statistically uniform fields within the fairing cavity. A removable payload model and a payload adapter model are included in the fairing to study the interactions of fields with these structures. Acoustic and RF absorbing foams and blankets are used in the fairing model to represent actual launch vehicle environments. Power balance model suggests that different regions of the fairing can be modeled as separate resonant cavities with energy transferring between them. This study investigates the quality factor (Q) measurement of the payload fairing sub-regions to verify the application of power balance model in payload fairings. The quality factor of the empty fairing measured from about 32 dB at 1 GHz to 41 dB at 6 GHz. Measurement in three different regions of the fairing when no absorber was added yielded quality factors similar to that of the empty fairing, indicating that the fairing behaves as single resonant cavity. After adding the absorbers, the quality factor measured in the fairing sub-regions were significantly reduced, indicating that the three regions of the fairing behave as separate but coupled cavities as expected from the power balance model.

TABLE OF CONTENTS

Chapter	Page
I. INTRODUCTION.....	1
II. REVERBERATION THEORY OF ELECTROMAGNETIC FIELDS.....	6
2-1 ELECTROMAGNETIC FIELDS IN CAVITIES	7
2-2 STATISTICAL THEORY OF REVERBERATION CHAMBER	9
2-3 FIELD STIRRING IN RESONATING CAVITIES	13
2-4 THE QUALITY FACTOR OF REVERBERATION CHAMBER.....	14
III. PAYLOAD FAIRING SCALE MODEL	19
3-1 PAYLOAD FAIRING SCALE MODEL.....	19
3-2 FABRIC PANEL STUDY	23
3-3 ALUMINUM & CU-NI FABRIC TEST BOX	31
3-4 CU-NI FABRIC TEST BOX.....	35
3-5 ASSEMBLY OF THE PAYLOAD FAIRING.....	3
IV. PAYLOAD FAIRING SUPPORTING ARTICLES	43
4-1 FAIRING MECHANICAL STIRRER.....	44
4-1a TUNER ASSEMBLY.....	49
4-2 PAYLOAD & PAYLOAD ADAPTER	52
4-2a PAYLOAD ADAPTER.....	56
4-3 FIELD PROBE.....	58
4-3a FIELD PROBE ASSEMBLY	59
4-4 ELECTROMAGNETIC SHIELDING GASKETS.....	63
4-5 ACOUSTIC & RF ABSORBING FOAMS	66

Chapter	Page
V. QUALITY FACTOR MEASUREMENT RESULTS	68
5-1 ETS-LINDGREN SMART-80 REVERBERATION CHAMBER	68
5-2 PAYLOAD FAIRING QUALITY FACTOR	73
5-3 QUALITY FACTOR IN FREQUENCY-DOMAIN.....	76
5-3a REFLECTION COEFFICIENT IN REVERBERATION CHAMBER	77
5-3b ANTENNA EFFICIENCY	79
5-3c CORRECTION FACTOR	81
5-3d PAYLOAD FAIRING Q IN FREQUENCY-DOMAIN	83
5-4 PAYLOAD FAIRING Q WITH SINGLE ANTENNA	86
5-5 LOSSY OBJECT IN PAYLOAD FAIRING	87
5-6 SPACECRAFT MODEL WITHIN THE FAIRING	91
5-7 FIELD PROBE MEASUREMENT OF Q.....	93
5-8 FAIRING LOCAL CAVITY Q WITH ABSORBERS	96
VI. CONCLUSION.....	103
REFERENCES	105
APPENDICES	108

LIST OF TABLES

Table	Page
Table 1: PAYLOAD FAIRING MODEL STRUCTURAL COMPOSITION	23
Table 2: NEMA 17 STEPPER MOTOR SPECIFICATIONS.....	50
Table 3: FIELD PROBE ASSEMBLY COMPONENTS SUMMARY	63
Table 4: ACOUSTIC ABSORBER FOAM (BASF MELAMINE)	66
Table 5: RF ABSORBING FOAM (MF11 -0002-00).....	67
Table 6: MR21-0001-01	67
Table 7: ETS-LINDGREN SMART-80 CHAMBER SPECIFICATIONS.....	69
Table 8: SUMMARY OF QTD MEASUREMENTS.....	75
Table 9: SUMMARY OF SINGLE ANTENNA Q.....	87

LIST OF FIGURES

Figure	Page
Figure 1: Typical Launch Vehicle Payload Fairing Configuration	3
Figure 2: Local Regions in Payload Fairing	4
Figure 3: Electromagnetic Compatibility Test Setup in RC	11
Figure 4: Payload Fairing Scale Model Dimensions	20
Figure 5: Horizontal Layout Showing Fairing Wall Composition	21
Figure 6: Sideway of Fabricated Fairing Half	22
Figure 7: Cu-Ni Fabric Over Fiberglass Test Panel.....	23
Figure 8: Reflection Measurement of the Test Panel.....	24
Figure 9: Small Anechoic Chamber Panel Test Setup.....	25
Figure 10: Cu-Ni Shielding Fabric Reflection.....	26
Figure 11: Reflection Comparison of Cu-Ni Fabric & Aluminum Panel.....	27
Figure 12: The Effects of Conductive Paint on EM Reflection.....	28
Figure 13: Attenuation of EM Energy Transmitting through Test Panels.....	29
Figure 14: S21 Measurement for the Three Different Test Panels	30
Figure 15: Avionics Box Model Resembling a Small-Scale RC.....	32
Figure 16: Aluminum Test Box with Front Panel Removed	33
Figure 17: Two Port Quality Factor Measurement Setup.....	34
Figure 18: S21 Energy Density Rate for the Aluminum Test Box	35
Figure 19: Making of the Rectangular Cu-Ni Test Box	36
Figure 20: Cu-Ni Fabric Box Modeling the Avionics Box.....	37
Figure 21: S11 Energy Decay Rate in Cu-Ni Fabric Box.....	38
Figure 22: Payload Fairing Half Fabricated at OSU.....	39
Figure 23: Payload Fairing Scale Model Final Assembly	40
Figure 24: Space Availability within the Payload Fairing Model	41
Figure 25: Mechanical Stirrer Used in the Payload Fairing	44
Figure 26: Fairing Tuner Dimensions in Inches	45
Figure 27: Sketch of the Tuner Placement Drawn to Scale.....	46
Figure 28: Rough Sketch of the Tuner Placement	47
Figure 29: Fairing Tuner Installed in the Top Cavity	48
Figure 30: Tuner Assembly with the Stepper Motor	49
Figure 31: Rough Sketch of the Tuner Assembly.....	51
Figure 32: Actual Tuner Assembly Built for the Mechanical Stirrer	52

Figure 33: Cylindrical Payload Model.....	53
Figure 34: Fairing Local Regions	54
Figure 35: Payload Fairing Scale Model Dimensions	55
Figure 36: Final Assembly of the Payload & Payload Adapter.....	57
Figure 37: 5 cm & 10 cm Dipole Probe.....	59
Figure 38: Field Probe Assembly Components	60
Figure 39: 10 cm Rigid Coax Cable	61
Figure 40: Field Probe Placement on the Fairing Wall.....	62
Figure 41: EM Shielding Gasket Types.....	64
Figure 42: Tech-Etch 2400 Series Fabric over Foam	64
Figure 43: Gaskets Installed on the Fairing Flange	65
Figure 44: Single Layer of Conductive Adhesive Tape.....	65
Figure 45: SMART-80 Chamber Q Measurement Setup	70
Figure 46: SMART-80 Time-Domain Q at 1 GHz.....	71
Figure 47: Power Decay Profiles for SMART-80 Chamber.....	72
Figure 48: Measurement Setup for Time-Domain Q.....	74
Figure 49: Empty Fairing Q at 1 GHz using 18 Tuner Positions.....	75
Figure 50: Empty Payload Fairing Cavity Power Decay Profile.....	76
Figure 51: Reflection Coefficient of the Dual-Ridge Horn Antenna.....	77
Figure 52: Reverberation Chamber Reflection Coefficient	78
Figure 53: Antenna Reflection Coefficient Measurement in Fairing	79
Figure 54: Dual-Ridge Horn Antenna Efficiency in RC & AC.....	80
Figure 55: Horn Antenna Efficiency Measurement in Fairing	81
Figure 56: Dual-Ridge Horn Antenna Correction Factor in RC.....	82
Figure 57: Dual-Ridge Horn Antenna Correction Factor in Fairing.....	83
Figure 58: Frequency-Domain Q Measurement of Empty Fairing.....	84
Figure 59: QFD Compared to QTD Values for Empty Fairing	85
Figure 60: Single Antenna Power Decay Profile of Empty Fairing	86
Figure 61: Cardboard Used as Support to Place the Antenna.....	88
Figure 62: QTD of the Payload Fairing with the Moist Cardboard.....	89
Figure 63: Fairing Single Antenna Q in Frequency & Time Domains.....	90
Figure 64: Payload Model Placed Within the Fairing Cavity	91
Figure 65: Q of the Fairing with the Payload	92
Figure 66: Reflection Coefficient of 5 cm Dipole in RC.....	94
Figure 67: Reflection Coefficient of 10 cm Dipole in RC.....	95
Figure 68: Fairing Local Cavity Q with Payload.....	96
Figure 69: Acoustic Absorbing Foam and RF Absorbing Foam	97
Figure 70: Final Assembly of the Absorbing Foams	98
Figure 71: Local Bottom Cavity of the Payload Fairing.....	99
Figure 72: Local Middle Cavity of the Payload Fairing	100
Figure 73: Local Top Cavity of the Payload Fairing	101
Figure 74: Frequency-Domain Q for the three local regions.....	102

CHAPTER I

INTRODUCTION

The payload within the fairing of a launch vehicle is exposed to various sources of electromagnetic field during ascent to space. These sources can be internal such as telemetry transceivers on board the launch vehicle or payload or external sources such as radar signals used by civil and defense aviation, communication satellites signals, long range AM radio waves and others [1]. Launch vehicles are designed to transport the payload safely and efficiently to space. This requires the use of a payload fairing, a cylindrical enclosure that shields the payload from acoustical vibrations, aerothermal heating, aerodynamic loading, and contamination during ascent while maintaining aerodynamic efficiency. In doing so, the fairing creates an electromagnetic interference problem for the payload as the fairing's metallic enclosure creates a resonant cavity where electromagnetic fields can build up to high levels [2]. The large field levels are established because numerous cavity field resonant modes build up within the fairing. When the resonances overlap and the fields interfere constructively, the electromagnetic fields can reach potentially high levels that can harm the payload's electronic systems. Both internal and external sources can lead to the build-up of the high intensity cavity fields within the fairing.

The space industry, during its early decades, overlooked fairing research to understand the interactions between electromagnetic fields and the payload. Early payload (crewed spacecraft or satellite) electronic systems used circuits that were less sensitive to the fluctuations of

electromagnetic fields in their vicinity. In addition, fewer large size transistors were used in early integrated circuits. The operating RF frequencies used by the launch vehicle communication systems were also moderately lower compared to today's standards [2]. In modern payloads, the electronic systems operate in higher frequency ranges while employing more and ever smaller transistors which make them highly susceptible to fluctuations of interfering electromagnetic fields.

Propagating fields with low energy density penetrate the fairing enclosure and are coupled into the fairing cavity to establish resonant fields with high energy density. The electromagnetic fields in a reverberant cavity undergo multipath propagation by reflecting off the cavity walls. The multipath fields interfere constructively or destructively, creating standing or reverberant electromagnetic fields. Large levels of resonant fields in the fairing increase the risk of electromagnetic interference and susceptibility to electronic systems of the payload. The fairing contains multiple structures and materials within its cavity besides the payload such as the payload adapter, various types of protecting foams including acoustical absorbing foams, and RF shielding blankets. The absorbing materials suppress acoustic vibrations and excess RF energy in the fairing experienced by the vehicle during ascent. The acoustic foams protect the payload from strong acoustical vibrations permeating in the launch vehicle structure. These objects within the fairing can affect the field structure around them.

The sketch in figure 1 shows a typical launch vehicle and payload fairing design used in the space industry. The payload fairing cavity can be divided into three regions or sections for analysis. These regions will be referred to as local cavities in subsequent chapters. The region above the payload or nose section, the middle region where the payload is placed, and the payload adapter section that is the lower cavity within the fairing.

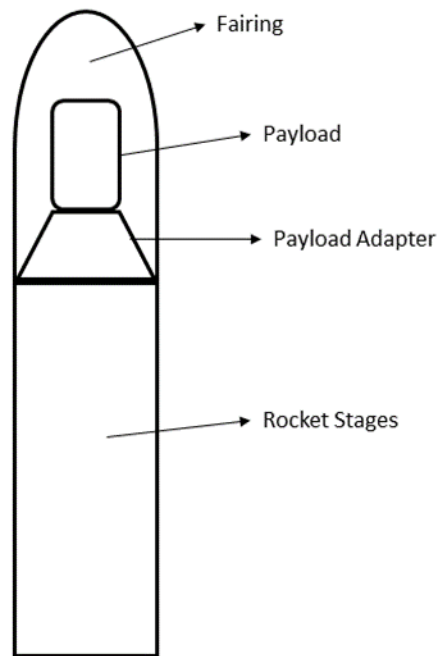


Figure 1: Typical Launch Vehicle Payload Fairing Configuration

The central region of the fairing with the payload is different in volume and shape than the upper cavity, which has more empty space. This study looks at the configuration disparity within the fairing regions and assesses if it has pronounced effects on the overall field structure and quality factor of the resonant electromagnetic modes within the fairing.

The field level established in the payload fairing is proportional to the quality factor of the fairing cavity resonances. The quality factor (Q) is a real, positive value at single frequency that shows the ability of the cavity to store resonant energy. Local measurements of the quality factor in each cavity are needed to analyze the effects of lossy objects and other structures placed within the fairing. The three regions of the fairing can be modeled as separate resonant cavities with energy transferring between them. Power injected into one region can propagate into other regions. Bremner et al [4] have suggested the application of power balance model to examine the flow of

energy between reverberant cavities. The power balance model has previously been used by Hill [5] to determine the shielding effectiveness and energy decay time of cavities with apertures. Nonetheless, finding the Q value of any reverberant cavity is one of the first steps in electromagnetic compatibility treatment of an EUT (Equipment Under Test) that may be placed in the cavity. The quality factor of the fairing will be measured in each sub-cavity to assess the effects of the payload and payload adapter on the field configuration. Different field levels can be expected in each region.

A scale model payload fairing has been fabricated at the Oklahoma State University Robust Electromagnetic Field Testing and Simulation (REFTAS) laboratory, to represent a realistic model of the electromagnetic environment in actual payload fairings.

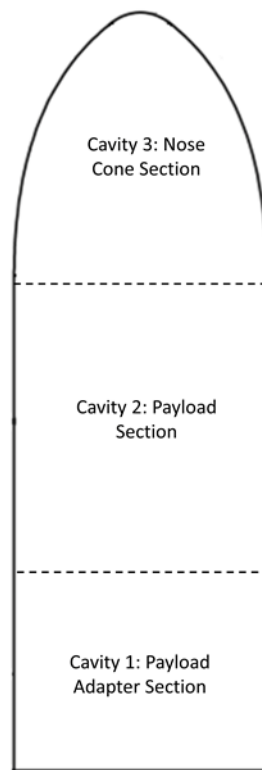


Figure 2: Local Regions in Payload Fairing

Local measurement of quality factor can be conducted to assess the effects various loss mechanisms such as wall losses, absorption, aperture leakage and antenna efficiency loss in each sub-cavity of the fairing.

The OSU fairing is made out of fiberglass and with a conductive fabric layer added to provide shielding. An earlier effort had used aluminum foil to shield a non-metallic composite fairing fixture [2]. However, the aluminum foil was simply attached to inner surfaces of the fairing, and proved to be challenging for getting a smooth conductive surface.

The OSU fairing model is electromagnetically large at the test frequencies (1 to 6 GHz), allowing multiple resonant modes to be established simultaneously. A mechanical tuner has been placed in the nose section of the fairing. The tuner or stirrer rotates around its axis, changing the cavity boundary conditions that results in producing different resonant modes within the fairing. Fixed resonant modes are established without the tuner. However, the tuner redistributes the energy to different resonant modes, giving unique realizations of the resonant fields allows the determination of the statistics of the resonant fields under random conditions. A removable payload model and a payload adapter model are included in the fairing to study the interactions of fields with these structures. The statistical theory of reverberation chamber [5] is selected as theoretical framework to analyze the electromagnetic cavity fields in the payload fairing.

Chapter Two presents a brief overview of reverberation theory of electromagnetic fields. Chapter Three details the design of the payload fairing scale model. The mechanical tuner, payload model, and field probe assembly are discussed in Chapter Four. Chapter Five presents the quality factor measurements of the fairing cavity total volume, and the Q of each sub cavity. The final chapter states the conclusions reached about the characterization of electromagnetic fields within the launch vehicle payload fairing.

CHAPTER II

REVERBERATION THEORY OF ELECTROMAGNETIC FIELDS

The literature for an effective theoretical description of resonant fields in the payload fairing cavity is reviewed here. First, a brief account of deterministic approach to solve EM field problem in a simple cavity is discussed. Typically, resonating cavities are designed to operate in single-mode configuration, but the simultaneous resonance of multiple-modes is possible. The size and quality factor of the cavity determine the number of modes that can be established at a single frequency. A multi-mode resonator, usually a rectangular cavity, can be used as test environment known as a reverberation chamber. The multimodal electromagnetic environment beneath a launch vehicle fairing also behaves as a reverberation chamber.

The fields in reverberation chamber are described by a statistical theory which is reviewed in section two of this chapter. The chamber has numerous cavity field modes. However, the placement of a mechanical stirrer changes the modal structure and excites new resonating cavity modes. The stirrer is typically a z-shaped metal surface that can be rotated incrementally. Each rotational position of the stirrer excites some modes but leaves many modes with small excitation. An ensemble average of field measurements at each stirrer position is used to capture all possible cavity modes that can be significantly excited. The concepts of field stirring and modal density which are the underlying principles of reverberation theory are explained in section three. The quality factor is another important parameter for determining the field strengths that are

established within the fairing cavity. It shows the relationship between stored energy and power losses in a cavity. Analytical expressions for cavity Q both in deterministic and statistical theory are reviewed in this chapter. Since the payload fairing is expected to have field properties similar to that in a reverberation chamber, the theoretical framework explored in this chapter is fully applicable to the payload fairing. The statistical theory of reverberation chamber will be used in following chapters to analyze the quality factor measurement data for the payload fairing.

2-1 ELECTROMAGNETIC FIELDS IN CAVITIES

The electromagnetic field cavity effect is well-studied in three geometries that are most commonly encountered in engineering design, which are the rectangular, cylindrical, and spherical geometries. The characteristics of resonant cavities such as resonant frequency, field configuration, and cavity quality factor have been defined by analytical expressions using deterministic approaches. Maxwell's equations provide the framework to derive the Helmholtz wave equation. The method of separation of variable is applied to the wave equation to determine electric and magnetic fields that satisfy the boundary condition of the cavity [6]. These steps do not include any random variables and thus avoid a probabilistic description of the cavity fields.

Some of the analytical expressions of rectangular resonant cavities are presented here to be compared with the properties of a reverberation chamber in the next section. A general method for establishing cavity modes in rectangular resonators is to decompose the EM field into transverse electric (TE) or transverse magnetic (TM) fields in one of the three rectangular coordinate axes [5].

The resonant frequency of rectangular cavity is determined by

$$f_{mnp} = \frac{1}{2\sqrt{\mu\epsilon}} \sqrt{\left(\frac{m}{a}\right)^2 + \left(\frac{n}{b}\right)^2 + \left(\frac{p}{c}\right)^2} \quad (2.1)$$

where a, b, and c are cavity dimensions, μ and ϵ are magnetic permeability and electric permittivity respectively, $m = 0, 1, 2 \dots$; $n = 0, 1, 2 \dots$; $p = 0, 1, 2 \dots$, and noting that at least two of the three parameters (m, n, and p) must be non-zero to cover all possible TE and TM modes.

An important parameter for a microwave resonating structure is its quality factor value, or simply cavity Q. Pozar defines Q for a resonant circuit as [7]

$$Q = \omega \frac{\text{average energy stored}}{\text{energy loss/second}} = \omega \frac{W_m + W_e}{P_{loss}} \quad (2.2)$$

where ω is cavity operating frequency, W_m is energy stored in magnetic field, and W_e is stored electric energy.

This definition also directly applies to cavities where the energy is stored in electric and magnetic fields within the cavity enclosure, and the power loss occurs due to finitely conducting cavity walls and in the dielectric filling the cavity. General expressions for any cavity shape with only the wall and dielectric losses are [7]

$$Q = \left(\frac{1}{Q_c} + \frac{1}{Q_d} \right)^{-1} \quad (2.3)$$

where Q_c is the quality factor of cavity with only wall losses and Q_d is the Q of cavity with only dielectric losses. Q_c and Q_d are expressed as below

$$Q_c = \frac{2 \omega_0 W_e}{P_c} \quad Q_d = \frac{2 \omega W_e}{P_d} = \frac{\epsilon'}{\epsilon''} = \frac{1}{\tan \delta}$$

where P_c and P_d are power losses due to conductive walls and dielectric filling respectively, and $\tan \delta$ is the loss tangent of the dielectric filling material.

The deterministic, theoretical approach to determine the quality factor given so far is not convenient to apply in complex cavity structures such as the payload fairing. Limitations of deterministic analysis and the motivation for a statistical approach in electrically large cavities are presented in the next section.

2-2 STATISTICAL THEORY OF REVERBERATION CHAMBER

As noted, a typical payload fairing cavity is electrically large. The conductive surfaces of the fairing enclosure perturb, or “scatter”, the electromagnetic fields inside the cavity. Structures such as the payload and payload adapter also perturb the fields. Many techniques have been developed for deterministic analysis of scattered fields such as geometrical theory of diffraction and physical theory of diffraction, moment method, finite element method, and modal techniques [6]. The payload and payload adapter inside the fairing also introduce power losses (conductive loss). Other sources of power loss (absorption) are RF absorbing materials that are applied to the inner cavity walls of the fairing to protect the payload. These materials have both conductive and dielectric losses. These losses can be obtained using the complex permittivity and electrical conductivity of the materials [6]. An accurate description of these loss mechanisms is needed to determine the field configuration in payload fairing with the deterministic approach.

It is challenging to represent all the field perturbations and energy losses from structures and materials analytically inside the fairing. Commercial numerical 3D wave software packages such as Computer Simulation Technology (CST) and High Frequency Structure Simulation (HFSS) can be used to solve complex cavity field problems where multiple field perturbation and lossy materials are present. These software packages are accurate and robust, but they are limited to the modeling of sufficiently small electrical environments. The payload fairings used in the industry, usually ten or more meters in height, are very large electrically, considering that systems within the

farang may operate in the microwave range. The commercial 3D wave simulation packages require considerable computational and time resources which are not practical with current computer technology.

A different analytical approach is needed to treat complex absorbing and scattering objects in electrically large cavities. A well tested and verified approach is the statistical theory of reverberation chambers [5,8]. A reverberation chamber is an electrically large cavity with conductive walls where standing electromagnetic fields are established, exciting multiple cavity resonant modes simultaneously. The energy gets stored in the cavity volume as the electromagnetic fields are repeatedly reflected from the walls. The fields inside the reverberation chamber are stirred by a z-shaped, rotating conductive structure (mechanical stirrer) as depicted in figure 3.

The incident waves from transmitting source go through multiple reflections by hitting the conductive walls of the reverberation chamber, and the rotating tuner scatters the fields. These physical processes create a random electromagnetic environment inside the chamber where the field amplitude, phase, and polarization of the field can no longer be effectively described deterministically. As a result, the fields become isotropic with no overall direction of propagation or specific polarization. Reverberation chambers are generally used for electromagnetic compatibility (EMC) tests. Without a reverberation chamber, EMC test can be conducted by a single source antenna, illuminating the test article by slowly sweeping through the frequency range of the operation. However, the test articles in reality would be exposed to a complex RF environment made up many frequencies and field configurations that are constantly changing. A reverberation chamber establishes a realistic operating environment in the lab for EMC testing. Figure 3 shows a common setup of electromagnetic interference and susceptibility test for an electronic device in a reverberation chamber.

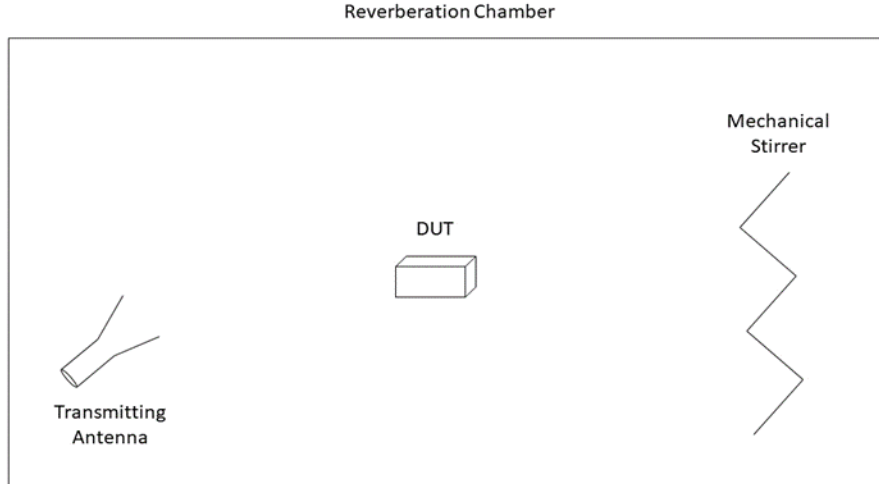


Figure 3: Electromagnetic Compatibility Test Setup in Reverberation Chamber

Reverberation chamber theory is built on the assumption that a statistically uniform field can be generated inside the chamber. Many stirrer positions are used to excite multiple resonant modes within the chamber as the stirrer is rotated in small increments. Each unique position of the stirrer effectively alters the boundary conditions of the chamber, exciting different resonant modes. Once the statistical uniformity of the fields inside the chamber is achieved, it must be compatible with Maxwell's equations. The theoretical approach must incorporate statistical uniform fields into Maxwell's equations. Hill uses [9] a plane-wave integral representation of the fields to meet both Maxwell's equations and the statistical properties of the reverberation chamber.

The sum of a spectrum of plane waves in the reverberation chamber environment is represented below [5]

$$\bar{E}(\vec{r}) = \iint_{4\pi} \bar{F}(\Omega) \exp(i\vec{k} \cdot \vec{r}) d\Omega \quad (2.4)$$

where Ω is the solid angle including the elevation and azimuth angles, α , β . Equation 2.4 represents a superposition of uniform plane waves propagating in all directions. Within a stirred reverberation chamber, $\bar{F}(\Omega)$ is a complex random variable that gives the amplitude of each plane wave. Stirring of the chamber redistributes that chamber field, randomly changing $\bar{F}(\Omega)$ for all values of Ω . The fields within the reverberation chamber are described by statistical ensemble averaging over different stirring samples. The mean field is

$$\langle \bar{E}(\vec{r}) \rangle = \iint_{4\pi} \langle \bar{F}(\Omega) \rangle \exp(i\vec{k} \cdot \vec{r}) d\Omega = 0 \quad (2.5)$$

where $\langle \rangle$ is ensemble average over stirrer or tuner positions. The ensemble average of electric field is zero in a reverberation environment where the multipath waves have random amplitude due to constructive and destructive interference. The random phase occurs when multipath waves travel different random distances before reaching the test point. However, the absolute value of electric field, which determines the electromagnetic energy density, is considered. The mean electric energy density within the chamber determines the field magnitude in cavity enclosures such as the payload fairing. Therefore, the mean-square value of the electric field is found by taking the ensemble average of the magnitude-squared electric field. Hill shows the mean-square electric field as

$$\langle |\bar{E}(\vec{r})|^2 \rangle = 4C_E \iint_{4\pi} d\Omega_2 = 16\pi C_E \equiv E_0^2 \quad (2.6)$$

where C_E is defined as the mean-square value of electric field for convenience. The energy density E_0^2 is independent of position inside a well-stirred reverberation chamber.

2-3 FIELD STIRRING IN RESONATING CAVITIES

The electromagnetic fields in rectangular and cylindrical cavities can be stirred by the z-shaped metal stirrer which changes the resonant frequencies of the cavity as it is rotated to unique positions around its axis. The statistical theory of reverberation chamber is valid when a high number of modes are excited within the cavity. The cavity is referred to as over-moded in this case. In the over-moded case, there are sufficiently high number of resonant modes established to ensure the randomness of the field amplitude, phase, and polarization. The statistically uniform field within the cavity is established by constructive and deconstructive interference of the resonating fields.

The number of cavity modes also give an insight into the effects of scattering and power loss through apertures and absorption by different geometries in cavities. The payload fairing cavity includes acoustic absorbing foams and RF shielding blankets that wrap the payload, affecting the field configuration and respectively the excitation of cavity modes in the fairing. Additionally, the payload and payload adapter structures affect the cavity modes. There are analytical expressions that give the number of modes and modal density within cavities. The number of modes that can be established at or below a given frequency can be approximated as [5]

$$N_s(f) \cong \frac{8\pi f^3 V}{3c^3}, \quad (2.7)$$

where V is the cavity volume, and c is the speed of light through the dielectric filling of the cavity. Equation (2.7) is a smoothed approximation of cavity mode number, hence the subscript s . The number of modes rapidly increases with increasing frequency. Another important parameter in the study of reverberation chamber is the modal density, given by

$$D_s(k) = \frac{dN_s(f)}{df} \cong \frac{8\pi f^2 V}{c^3}. \quad (2.8)$$

A higher modal density allows more cavity modes to be established at a single frequency at specific quality factor value. However, if the cavity Q lowers, the band over which a mode can be excited increases which also allows many modes to be established at a single frequency. High mode density is needed to get Rayleigh distribution of the fields and exponential distribution (Chi-squared with 2 degree of freedom) of the energy within the reverberant cavity [5].

The width of the modal response is determined by the quality factor of the chamber. A good analogy for reverberation chamber modal density is the quality factor curves of resonant circuits. A high-quality factor value has narrowband response whereas a lower Q is wideband and broadens the modal response. At lower frequencies in reverberation chamber, the Q value can be intentionally decreased by adding absorbers to get a wider modal response since the modal density is low for lower frequencies and a single operating frequency cannot excite multiple cavity modes at once. A well-stirred reverberant cavity at a single frequency will have numerous modes with different center frequencies operating at once.

2-4 THE QUALITY FACTOR OF REVERBERATION CHAMBER

The quality factor of a reverberation chamber shows how well the chamber stores the energy and whether large sources of power loss have been mitigated. The sources of power loss are chamber walls, power absorbed by objects in the chamber, losses through cavity apertures, and loading effect of antennas [11].

The chamber walls have surface resistivity that absorbs a small but quantitative amount of electromagnetic energy during each reflection and scattering of the fields from the walls. The absorbing objects can be the test articles under the study or structures that are part of the design of the chamber cavity. The payload fairing includes RF absorbing foams and blankets that lower the Q of the cavity. Any small aperture or seam in the cavity wall introduces power leakages. To

establish fields with high level of intensity for EMC tests in reverberation chambers, great effort should be placed in maintaining a continuously conductive surface in the reverberation cavity.

The quality factor is a single number at any given frequency. It indicates how dominant is the stored energy compared to cavity power losses. A higher Q means more energy is stored compared to the energy lost. The quality factor can be measured either in time-domain or frequency domain. In time-domain method, the chamber is excited by a pulse source and the field response is measured as received power vs time. Richardson has detailed this method in [8] using radar instrumentation. The received power vs time is displayed in the radar A-scope to allow the observation of the reverberant fields developing and eventually decaying.

Frequency-domain measurement relies on a continuous-wave (CW) source and receiver. Transmitting and receiving antennas are placed inside the chamber and the scattering-parameter (or S-parameter) data is collected by a vector network analyzer (VNA). However, the frequency-domain method has a disadvantage that it is affected by the efficiencies of the measurement antennas [11, 12, 13]. Both the loss and mismatch efficiencies of the antennas lower the measured quality factor. The Q measured in the frequency domain must therefore be corrected.

Hill presents an intuitive development of the analytical expressions for the calculation of quality factor from frequency domain measurements [5]. The quality factor is defined as

$$Q = \frac{\omega U}{P_d}, \quad (2.9)$$

where ω is operating angular frequency, U is the energy stored in the cavity and P_d is the power dissipated. In a well-stirred reverberant environment, the stored energy is randomly distributed within the cavity volume. The mean stored energy density inside the cavity is independent of position within the chamber volume.

In his development of quality factor expression in frequency-domain, Hill showed that the conservation of power, and steady state field conditions require that the power transmitted to the cavity equal the cavity power losses. By placing a well-matched and lossless receiving antenna in the chamber, it can be written that

$$\langle P_r \rangle = \frac{\lambda^3 Q}{16 \pi^2 V} P_t \quad (2.10)$$

where P_r is the mean power received by the antenna inside the chamber, P_t is the power transmitted into the chamber, V is the chamber volume, and λ is wavelength of the operating frequency. Equation (2.10) shows that a higher cavity Q gives a higher field strength measured by the received antenna for the same input power.

Launch vehicle fairings use various acoustic and RF blankets inside the fairing. In a comprehensive study of payload fairings, the acoustic and RF foams must be placed inside the fairing cavity, which can have significant impact on lowering the quality factor value. High conductivity materials should be used as the enclosure of the composite fairing to yield a high Q value, comparable to metallic fairings.

From equation (2.10), quality factor measured in the frequency-domain can be written as

$$Q = \frac{16 \pi^2 V \langle P_r \rangle}{\lambda^3 P_t} \quad (2.11)$$

Equation (2.11) applies to an impedance-matched and lossless receiving antenna. The quality factor can be written in terms of the scattering (S) parameters measured between two antennas within the cavity by a VNA [11]:

$$Q = \frac{16 \pi^2 V}{\lambda^3} \langle |S_{21}|^2 \rangle, \quad (2.12)$$

where S_{21} is the scattering parameter between the transmitting and receiving antennas.

Practical antennas have power loss efficiencies and power mismatch efficiencies that are less than unity. Imperfect antenna efficiency lowers the measured S_{21} , which is why the frequency-domain measured Q is lower than the time-domain measurement of the quality factor. The loss and mismatch efficiencies must be found and introduced in equation (2.12) to compensate for antenna efficiency loss.

The corrected frequency-domain quality factor that includes efficiency loss is

$$Q_c = \frac{Q}{\eta_1 \eta_2} \quad (2.13)$$

where η_1 and η_2 are the transmitting and receiving antennas efficiency. It is challenging to accurately define these efficiencies and calculate the Q using the frequency-domain measurements. Power loss of antennas are typically significantly smaller than the mismatch loss. Power losses are usually ignored while the mismatch losses are carefully measured through well calibrated microwave measurement system (VNA, cables, and connectors). The time-domain Q is not affected by antenna efficiency, which makes it a more favored method for the determining the quality factor of reverberant cavities such as the launch vehicle payload fairing.

West et al. [12] have employed Fourier theory to synthesize the pulse, time-domain response from VNA-based frequency-domain measurements. The frequency-domain data measured by CW instrumentation can be transformed to time-domain using an inverse Fourier transform. Then, the time-domain quality factor expressions suggested by Richardson in [8] can be used:

$$Q_{TD} = 2\pi f \tau_{RC}, \quad (2.14)$$

where τ_{RC} is the time constant of the chamber power decay and f is the operating frequency. The time constant τ_{RC} is determined by first finding the rate of decay of received power in the chamber by

$$\tau_{RC} = \frac{4.3429}{D}, \quad (2.15)$$

where D is the rate of power decay in dB/s.

Since the time-domain is concerned with the energy decay rate of the field in the cavity, the absolute levels of the field that are affected by antenna efficiencies do not matter. The absolute field level does not change the decay rate of the fields within the cavity. This technique effectively mitigates the challenges of measuring the efficiencies of the antennas for quality factor in frequency-domain. Comparing the frequency and time-domain Q measurement can be used to find the antenna efficiency [20].

There are two methods to find the quality factor in the time-domain. The Q can be determined by measuring the reflection from the input of a single antenna (S11) over multiple tuner positions [21]. Or, the quality factor can be found from the transmission (S21) between two antennas placed within the test [22].

CHAPTER III

PAYLOAD FAIRING SCALE MODEL

This chapter details the fabrication process and preliminary measurements of various aspects of the fairing scale model design such as the selection of material for the shielding enclosure and fairing dimensions. The composition of the fairing test article and design specifications are presented in section one. A set of preliminary S-parameters measurements for test panels were conducted to determine a substitute material instead of using aluminum to shield the fairing cavity. Measurement of a Cu-Ni electromagnetic shielding fabric showed comparable shielding performance to aluminum and is thus used in the fabrication of payload fairing for this study.

Section three includes measurements of a small avionics box of dimensions 30 x 30 x 12 cm to determine its quality factor. A rectangular test box of similar dimensions with the Cu-Ni fabric used as the shielding enclosure is compared the avionics box. The quality factor of the two boxes are compared to verify the performance of the electromagnetic shielding fabric. The chapter ends with a structural review of the fairing test article after its fabrication.

3-1 PAYLOAD FAIRING SCALE MODEL

The payload fairing scale model fabricated at Oklahoma State University is 2.44 m high with 0.8 m radius at its cylindrical section. The fairing has a total volume of 1.212 m^3 and total surface area

of 7.38 m^2 .

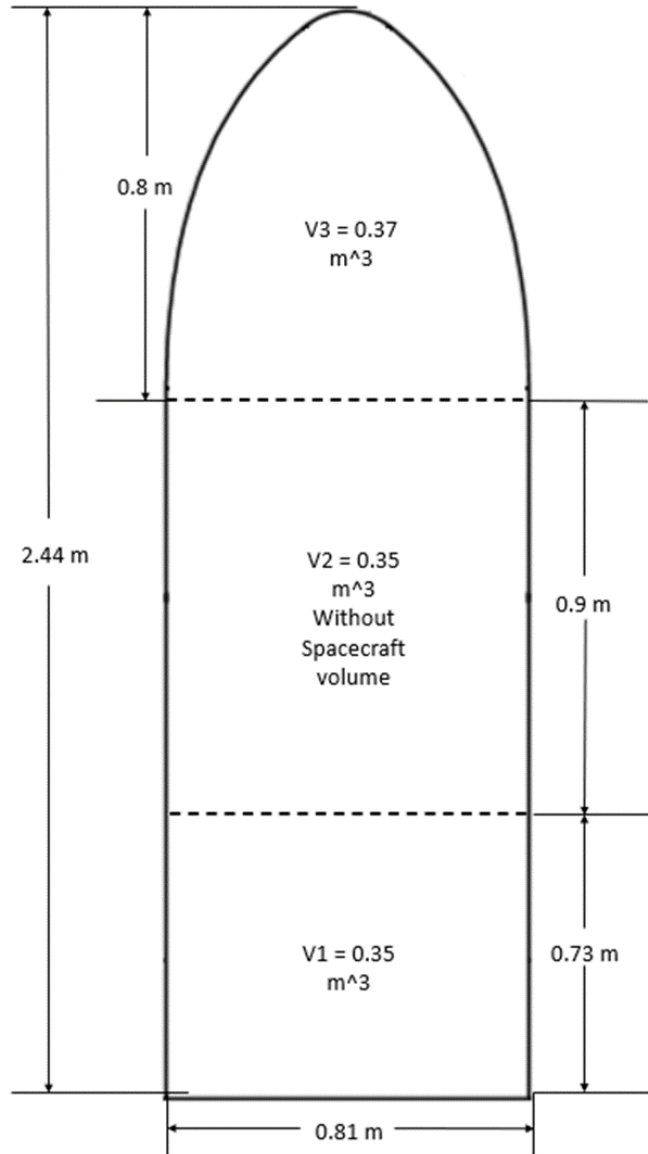


Figure 4: Payload Fairing Scale Model Dimensions

The fiberglass used in the OSU fairing is the 20oz Tooling Fabric of Tool Glass type manufactured by Fibre Glast. A layer of Divinycell Vinyl foam, also manufactured by Fibre Glast, is used in the

cylindrical section of the fairing to provide structural rigidity. The electromagnetic shielding was achieved using a conductive electromagnetic shielding fabric.

Metallic fairing scale models are too heavy and expensive to fabricate. Fiberglass or carbon fiber structures are light but do not have high conductivity to model actual payload fairings that are metallic. However, adding a conductive fabric layer to the fiberglass structure gives the needed conductivity while benefiting from a light fiberglass structure.

The fairing was fabricated by Oklahoma State University Mechanical & Aerospace Engineering department. A polished mold was prepared with the exact dimensions of the fairing scale model half. Layers of the fiberglass and vinyl foam were laid over the mold to make a fairing half shell.

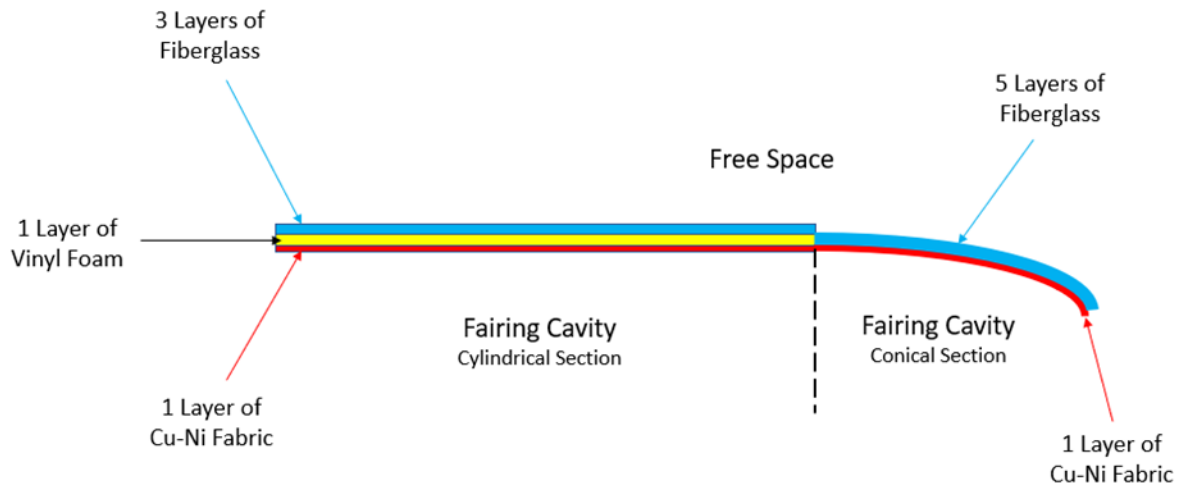


Figure 5: Horizontal layout showing fairing wall composition

As shown in figure 5, the cylindrical section has three layers of fiberglass and one layer of vinyl foam. The nose section uses five layers of fiberglass as the foam could not be shaped into conical shape smoothly. The fairing model is therefore slightly thicker (about 3 mm) in the cylindrical

section. A single layer of electromagnetic shielding material is used uniformly for both sections to form the conductive enclosure.



Figure 6: Left figure is the polished mold; right figure is sideview of fabricated fairing half

The conductive fabric used for this scale model is a copper-nickel polyester (Cu-Ni) cloth with 30 percent copper, 10 percent nickel, and 60 percent polyester. The surface resistivity of the fabric is 0.03 Ohm and is 0.1 mm thick. It is possible to have fairing models with no conductive fabric within the structure and tape aluminum foil to its interior for shielding [2]. But, the losses from the seams or any other joints of foil layers significantly lowers the cavity quality factor and thus renders the fairing ineffective for reverberant electromagnetic field studies of actual launch vehicle fairings.

The OSU payload fairing scale model is lightweight and can be easily lifted by a single person when its empty. This design allows rapid testing and measurement. The selection of composite materials and the Cu-Ni fabric for use in the fairing required preliminary measurements. Test panels composed of fiberglass, foam, and conductive fabric were fabricated to measure the reflectivity of the Cu-Ni fabric. Table 1 summarizes the materials used to build the fairing scale model at Oklahoma State University.

Product	Manufacturer	Specifications	Description
20oz Tooling Fabric	Fibre Glast	Thickness (0.8 mm) Breaking strength (Warp: > 52 n/mm, Fill: > 30 n/mm)	High strength characteristics, applicable to molds as back-up shell
Divinycell Vinyl Foam: 4 lb. Density	Fibre Glast	Thickness (9.5 mm) Shear strength (0.76 Mpa)	Used as sandwich core material in a composite part
Faraday Fabric – EMI RFID Shielding Earth Grounding	Amradiel	Surface resistance (0.03 ohm) Attenuation (85 dB from 30 MHz – 18 GHz)	Copper + Nickel + Polyster , diamond type, silver color

Table 1: Payload Fairing Model Structural Composition

3-2 FABRIC PANEL STUDY

Sample 30 x 30 cm panels were fabricated and tested for reflectivity in a small anechoic chamber.

Figure 7 shows the test setup of the panels. Three different sets of panels were fabricated:

- Cu-Ni fabric over fiberglass
- Conductive paint over fiberglass
- Cu-Ni fabric and conductive paint over fiberglass

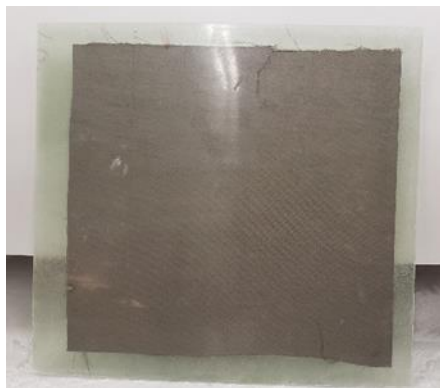


Figure 7: Cu-Ni Fabric over Fiberglass Test Panel (30 x 30 cm)

Additionally, two sheets of different aluminum alloys were also tested for reflectivity and shielding of the electromagnetic waves in the used frequency band. The horn antenna available for the panel tests was limited in frequency range to 3.3 GHz to 4.9 GHz. Therefore, all reflectivity and transmission measurements were conducted within this antenna frequency range. Figure 8 shows how the antenna and test panels were placed in a small anechoic chamber.

The reflectivity of the conductive fabric panels was evaluated by measuring the reflection, or S11 of the horn antenna. The calibration was performed at the cable end, making the antenna itself part of the test item. Similar setup was used for all of the test panel measurements. The antenna mismatch efficiency was present in every measurement so it can be ignored.

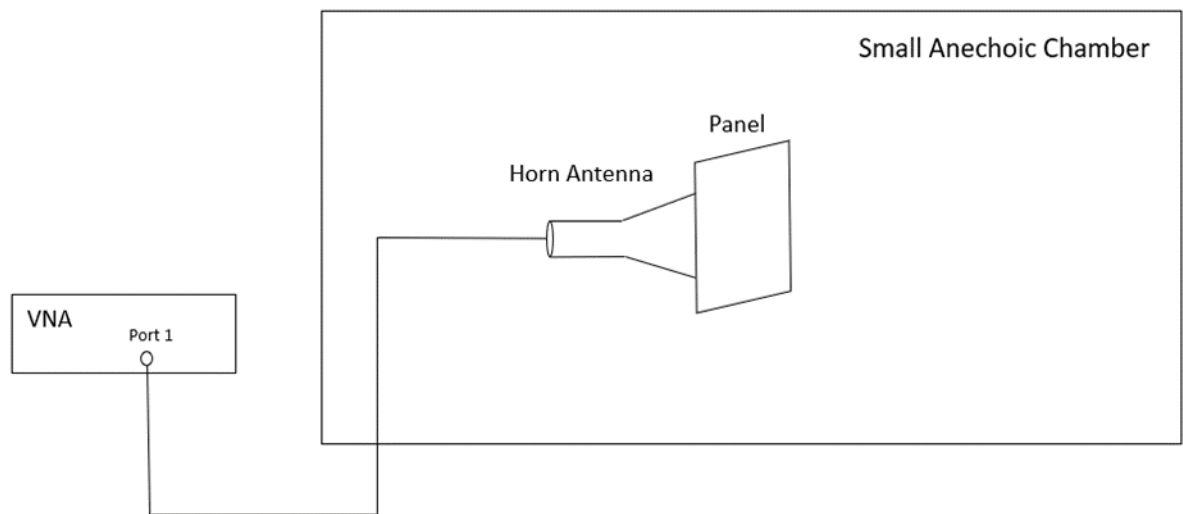


Figure 8: Reflection Measurement of the Test Panel

Figure 9 shows the horn antenna and test panel placed in a small anechoic chamber. The VNA cable was fed through a small hole in the bottom side of the chamber.

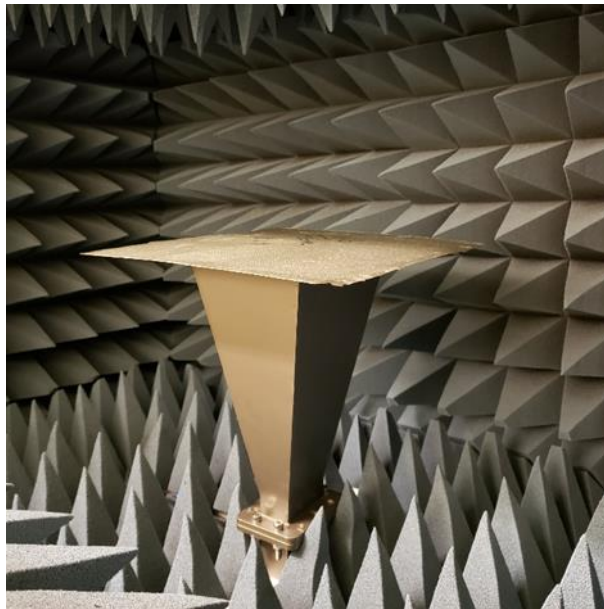


Figure 9: Small Anechoic Chamber Panel Test Setup

Figure 10 shows the reflection measured at the antenna power when the Cu-Ni fabric panel was placed across the horn aperture. The measurement was repeated four times with recalibration of cables between each measurement. Good repeatability is observed. Cavity resonances are observed between the horn antenna and panel. These resonances are not the subject of study here to understand the suitability of the conductive fabric for use as shielding in the fairing. They are ignored in subsequent discussion of the measurement plots.

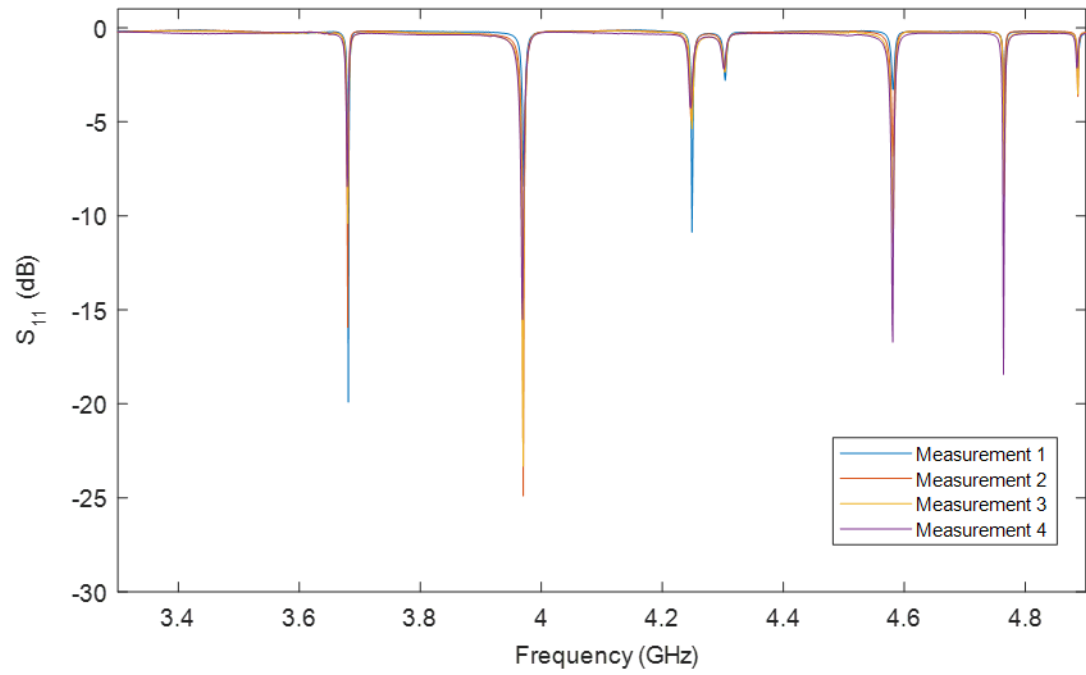


Figure 10: Cu-Ni Shielding Fabric Reflection

The reflectivity of the EMI fabric is compared with the reflectivity of an aluminum panel in figure 11.

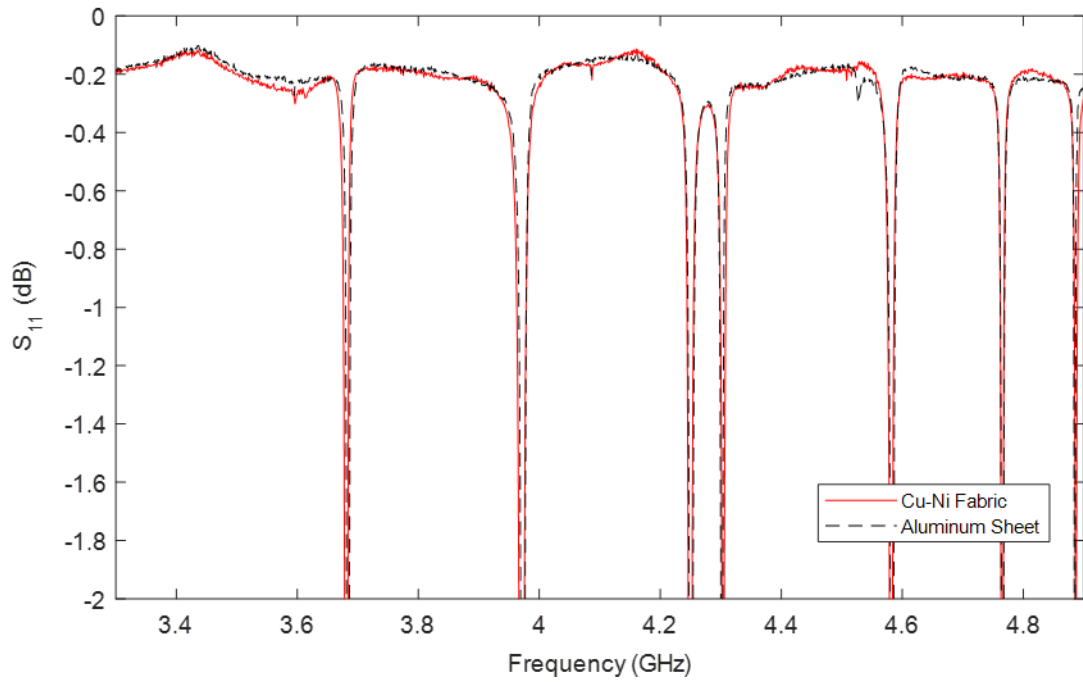


Figure 11: Reflection Comparison of Cu-Ni Fabric and Aluminum Test Panels

The fabric reflectivity is comparable to the reflectivity of aluminum. This result validates the use of Cu-Ni fabric for shielding in the payload fairing scale model fabricated at OSU.

Next, a conductive paint was added to the reflecting fabric panel, and a separate test panel was prepared with conductive paint over fiberglass, without using the EMI fabric. The paint was a nickel conductive paint for coating surfaces to reflect electromagnetic waves. Figure 12 compares the reflectivity of Cu-Ni fabric with and without the addition of conductive paint, and the test panel with only conductive paint over fiberglass.

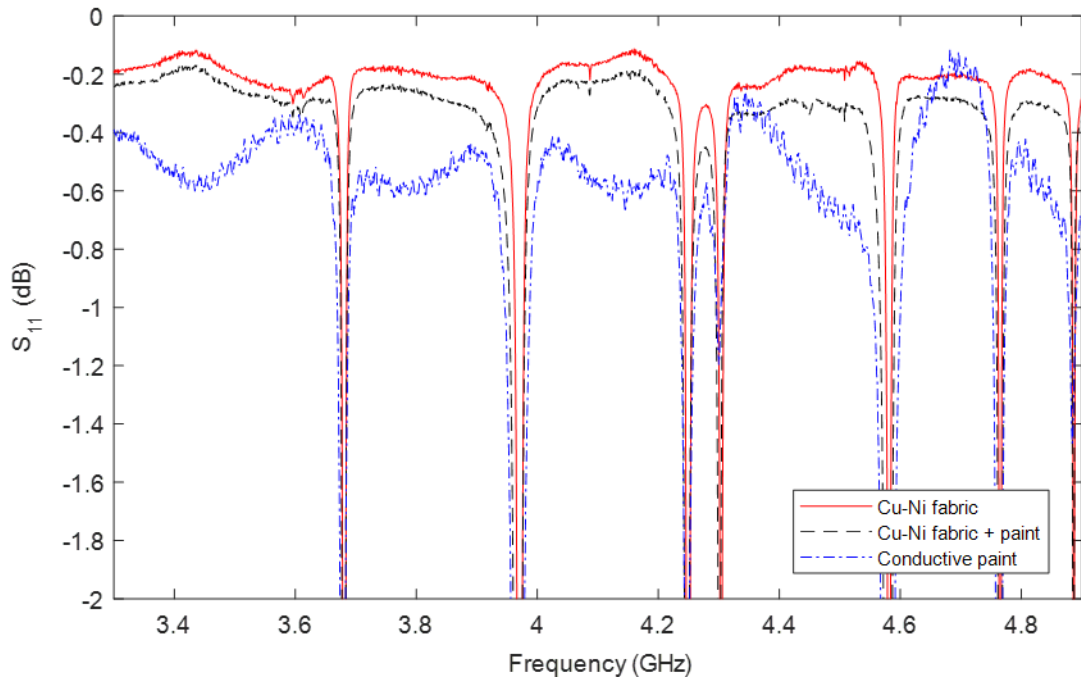


Figure 12: The Effects of Conductive Paint on EM Energy Reflection

The conductive paint shows strong reflection considering it is only a thin layer of conductive coating. However, its reflectivity is not as good as the Cu-Ni fabric panel. An interesting observation was that adding a conductive coating layer over the fabric actually lowered the reflectivity. The surface roughness or paint material losses can be the reason why the conductive coating lowered the wave reflection. The surface of the fiberglass panel with Cu-Ni fabric before applying the coating was smoother and when the paint was applied the surface became granular. Therefore, conductive coating was not used in the OSU fairing model.

The attenuation of transmitted electromagnetic energy through the Cu-Ni fabric panel was compared with an aluminum sheet using an S_{21} measurement. Figure 13 shows the test setup. S_{21} between the two horn antennas facing each other was measured with the test panels inserted between them.

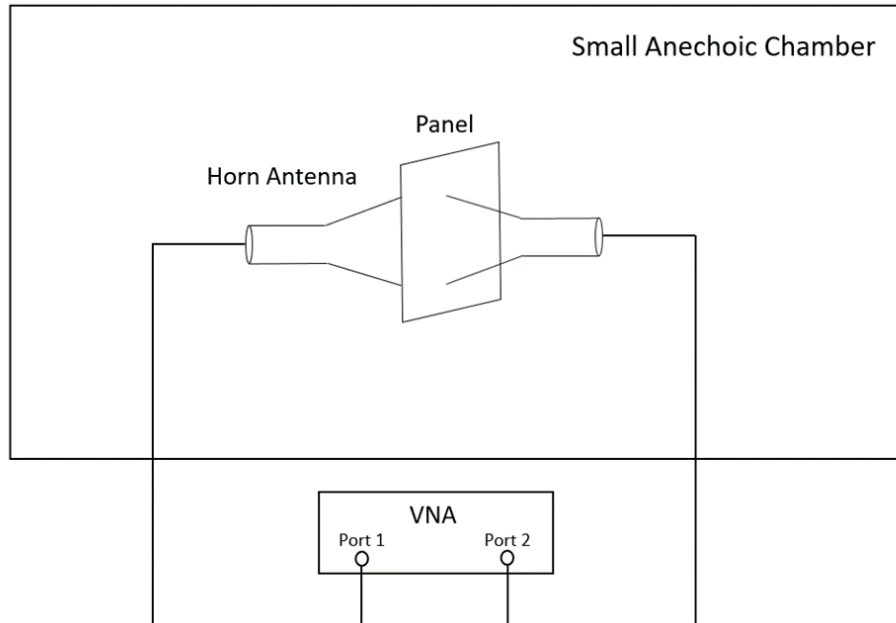


Figure 13: Attenuation of EM Energy Transmitting through Test Panels

The measured S_{21} for conductive fabric test panel is -65 dB, which is less than the -85 dB shielding effectiveness specification of the fabric.

The test setup for attenuation measurement in figure 13 is simple and mainly designed to verify an acceptable attenuation level of the fabric panels. Energy could be diffracting around the edge of the panel to the opposite side to receiving horn antenna, which would also be present for both fabric and aluminum test panels. It is not the objective of these tests to verify the specifications of the Cu-Ni fabric but rather to measure an acceptable attenuation level that is needed for the fairing scale model to represent the cavity environment of actual payload fairings.

Similar to S_{11} plots, the resonances in the cavity of the horn antenna is observed. The test panel is placed right next to the horn antenna, physically touching, and sealing its open end, and thus forming a cavity. Figure 14 shows S_{21} measurement for Cu-Ni fabric test panel, the aluminum sheet, and the panel with conductive paint over fiberglass.

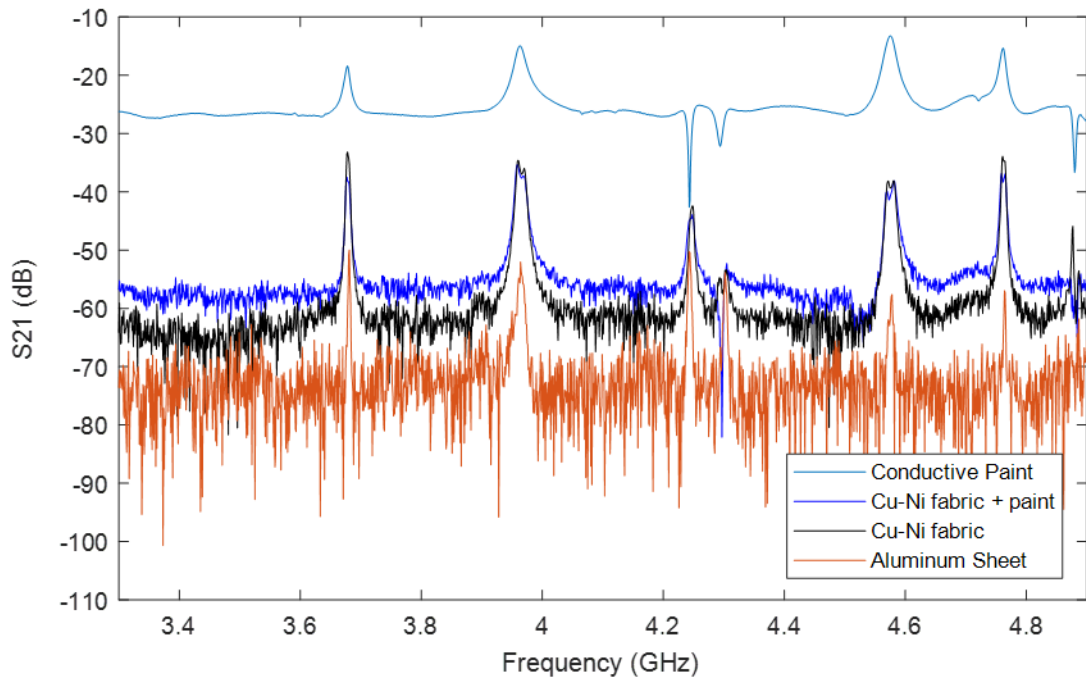


Figure 14: S21 Measurements for the Three Different Test Panels

Aluminum as expected gives the lowest measured S21 level (-75 dB). The Cu-Ni fabric follows aluminum relatively close, with 10 dB difference, noting that it is a composite product, made of copper, nickel and polyester. In figure 14, adding conductive paint over the Cu-Ni fabric does not improve attenuation as it did not improve reflectivity in above results.

The reflectivity and S21 measurements of the test panels with various configurations showed that the Cu-Ni fabric is an acceptable shielding material for the OSU model payload fairing. The fabric shielding and reflectivity approaches that of aluminum. It is also flexible and easy to shape in any form, making it a good choice for use in the OSU payload fairing scale model.

3-3 ALUMINUM AND CU-NI FABRIC TEST BOX

A small aluminum rectangular box has previously been used in shielding studies at Oklahoma State University. A rectangular box with similar dimensions of the aluminum box was fabricated from the Cu-Ni fabric for further study. The aluminum box was first tested to give a baseline for comparison with the fabric box performance.

The small box configuration is shown in Figure 15. It resembles avionics boxes used in airplanes or similar structures. It measures 30 x 30 x 12 cm. This test setup is used both for the aluminum test box and the Cu-Ni fabric test box. Both models are excited by a 10 cm monopole antenna. A mechanical stirrer is added in the box to achieve the statistical environment of reverberant electromagnetic fields within the box cavity through incremental rotations of the tuner. The z-shaped tuner is placed horizontally along the width of the box. It is built out of aluminum sheet and all-thread rod which is connected to the two sides of the box, supports the small tuner structure horizontally, and gives freedom of rotation. In this configuration, the cavity within the box behaves as a small reverberation chamber. Measurement of the cavity Q therefore gives insight to the electrical performance of the shielding material used to form the walls.

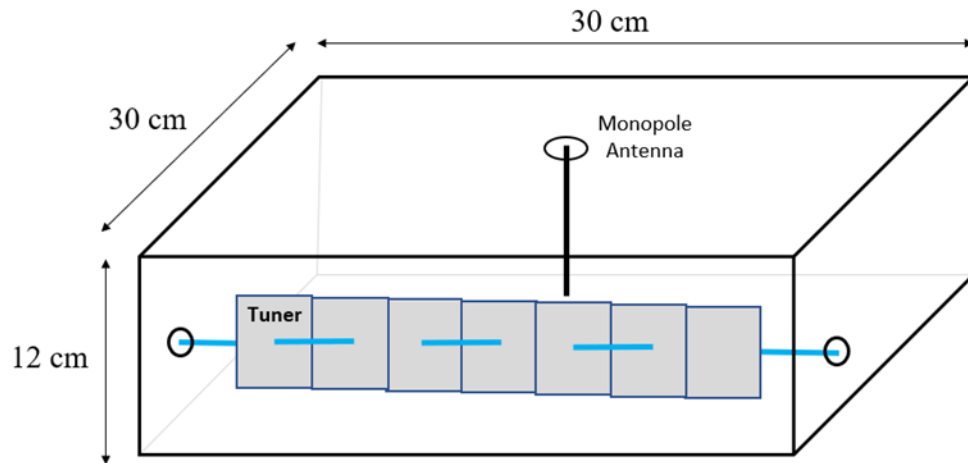


Figure 15: Avionics Box Model Resembling a Small-Scale Reverberation Chamber

A stepper motor outside of the box is used to rotate the tuner. It is connected to the tuner using a 5 mm diameter shaft that passes through a small hole in the enclosure wall. The shaft and coupler were chosen to insure mechanical rigidity during testing.

The stepper motor used for these measurements is the Nema 17 Closed Loop Stepper Motor [30]. It has a step angle of 1.8 degrees and has a torque of 45 N-cm. As the tuner is rotated by a stepper motor from the outside of the box, the all-thread rod grips the light-weight z-fold aluminum sheet, preventing it from slipping or vibrating as the tuner is rotated.



Figure 16: Aluminum Test Box with Front Panel Removed for the Observation of Small Tuner

Figure 16 shows the physical aluminum test box. The front panel of the box is removed to show the placement of the mechanical stirrer and monopole antenna.

The small avionics box is an under-moded cavity at low frequency operation due to the small modal density. The 10 cm length monopole wire antenna used to excite the field within the box consists of a piece of conducting wire soldered to the center pin of a female SMA PCB surface edge mount connector. It is fed through an SMA male to N-type female connector attached to the VNA test cable.

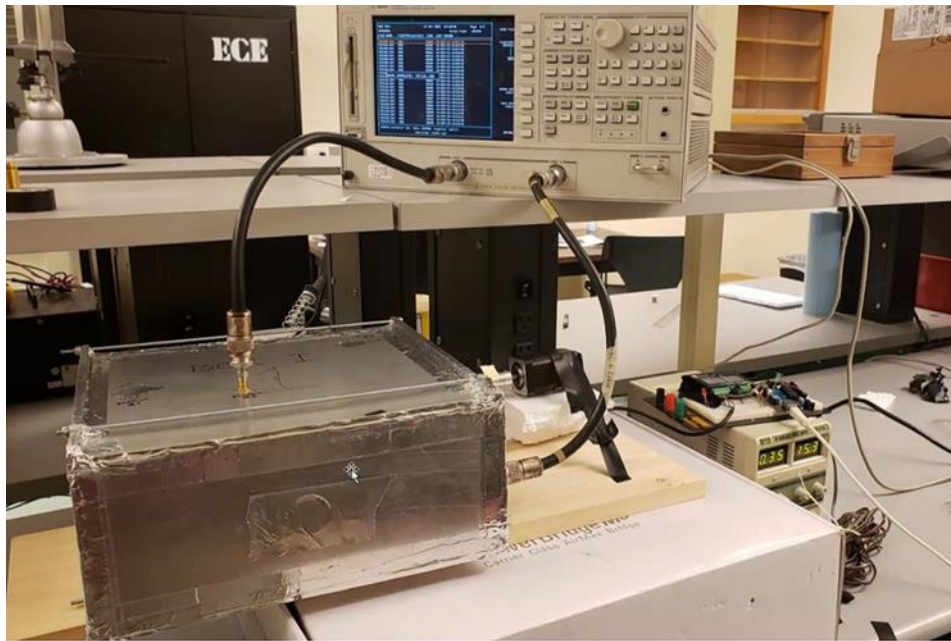


Figure 17: Two Port Quality Factor Measurement Setup for Aluminum Test Box

Figure 17 shows the test setup for a two-port time-domain Q measurement of the aluminum box. Two monopole antennas were used: one placed vertically and fed through the top of the box; the second antenna was placed horizontally entering the box from the side. The small z-fold tuner was rotated through 18 different tuner positions. The time-domain Q was determined using S21 measurement over a 100 MHz bandwidth centered at 5.55 GHz. The VNA was set to S21 at 1601 frequencies across the signal bandwidth.

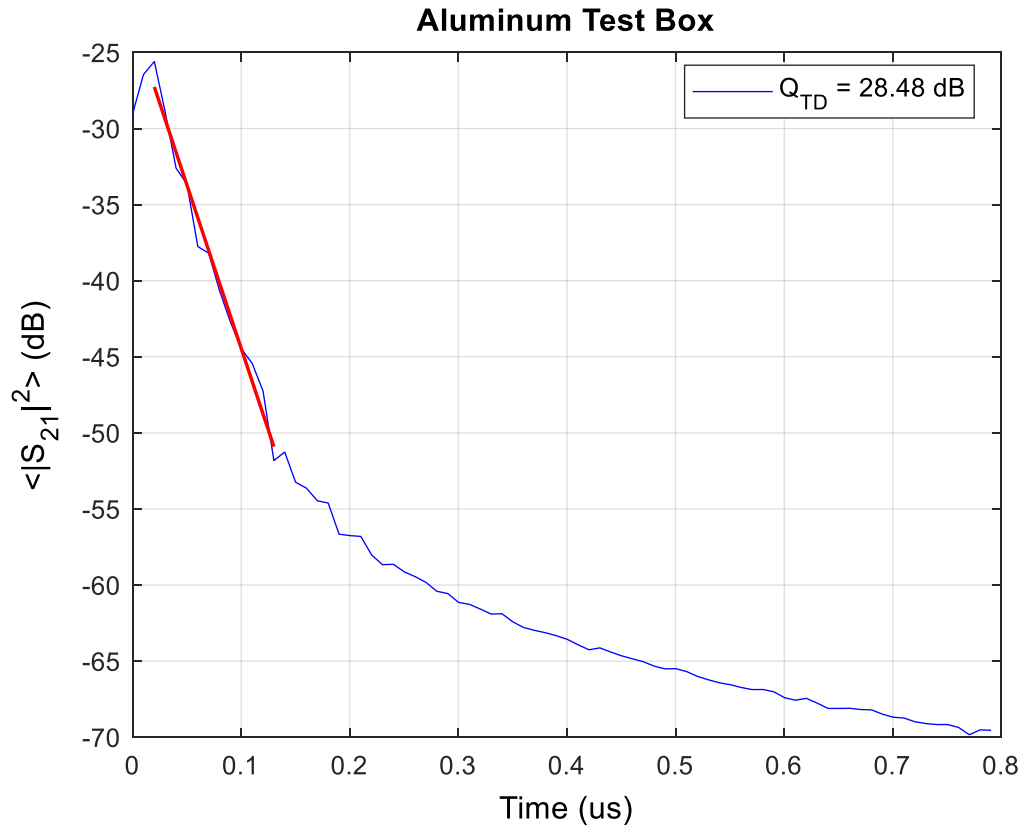


Figure 18: S_{21} Energy Decay Rate for the Aluminum Test Box

Figure 18 shows the aluminum test box energy decay. The red line shows a linear fit to the initial decay that is used to measure the quality factor. The decay rate is 86.33 dB/us. Using equations (2.15 and 2.14), the yields a Q of 28.5 dB. The pre-reverberant phase is extremely short as the energy rapidly dissipates in the wall losses and possibly escapes through possible seams in the structure. Smoothing of the walls of the test box did not raise the Q.

3-4 CU-NI FABRIC TEST BOX

A test box was built from the Cu-Ni fabric to compare its performance with the aluminum test box. The fabric box is similar in shape and dimensions to the aluminum test box of figure 15, with the

exception that an electromagnetically transparent Styrofoam structure is used to support the fabric walls. The dimensions of the box are 30 x 30 x 12 cm, similar to the avionics box, studied in the last section. Figure 19 shows the Styrofoam frame of the fabric box along with the placement of the small z-foiled mechanical stirrer.

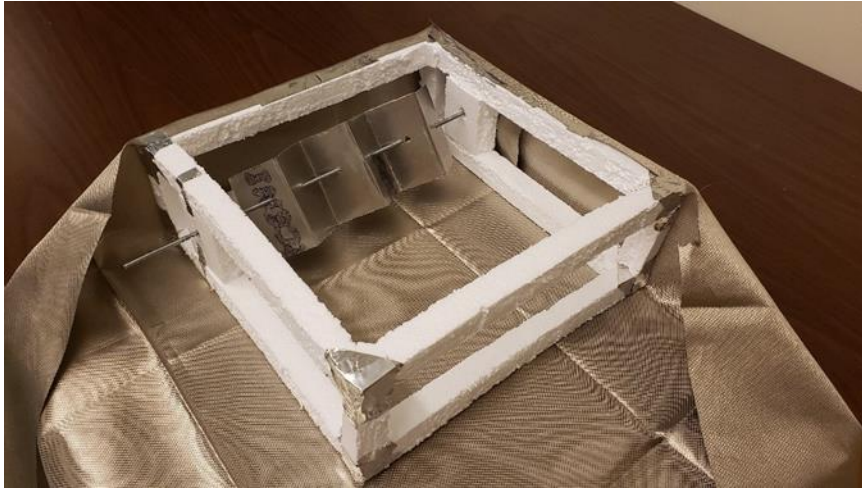


Figure 19: Making of the Rectangular Cu-Ni Test Box

After wrapping the foam around the frame, conductive adhesive aluminum tape was used to further seal the structure into a conductive cavity. The small tuner was secured by the frame itself on the two sides. The fabric test box was excited by a 10 cm monopole wire antenna fed through the fabric wall, similar to the configuration used with the aluminum box. The stepper motor was used to rotate the tuner in controlled step angles. The stepper motor also increased the stability of the tuner.



Figure 20: Cu-Ni Fabric Box Modeling the Avionics Box

The probe antenna was connected to the VNA port and S11 measurements were collected for eighteen different tuner positions. The quality factor of the Cu-Ni fabric test box was measured at 5.55 GHz center frequency and 100 MHz bandwidth. The measured Q value was 23.80 dB. It is 4.7 dB lower than the aluminum box but falls into acceptable range for the fabrication of the payload fairing. Use of the Cu-Ni fabric as the shielding layer in the fairing model is therefore validated.

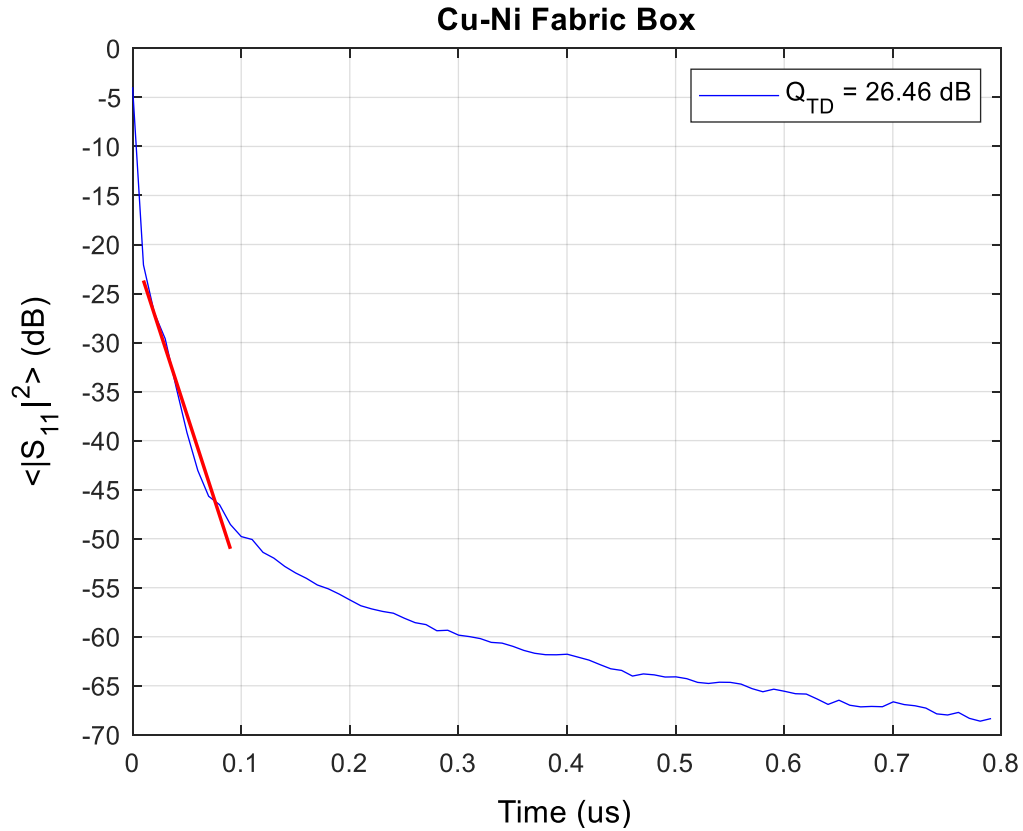


Figure 21: S11 Energy Decay Rate in Cu-Ni Fabric Box

3-5 ASSEMBLY OF THE PAYLAOD FAIRING

The fabricated payload fairing model is shown in Figures 22 and 23. The height of the model is 2.44 meters and its diameter at the cylindrical section measures 0.81 meters. These dimensions provide space to place a medium-sized mechanical tuner, surrogate payload, and payload adapter models, acoustic and RF absorbing foams, and finally measurements probes to determine the quality factor of the fairing.



Figure 22: Payload Fairing Half Fabricated by OSU Mechanical & Aerospace Engineering

The vinyl foam used for structural support in cylindrical section (yellow colored) is clearly visible in figure 23. The base of the fairing is hollow, but a cylindrical metallic base was separately built to provide the bottom of the fairing cavity. The circular base plate was simply made with a two-inch-thick plain wooden surface, overlaid with an aluminum sheet to get a conductive surface that will be exposed to the cavity fields.

The fairing model of figure 23 closely resembles an actual payload fairing used in launch vehicles that are built in two half shells and jettisoned once the vehicle leaves the Earth atmosphere.



Figure 23: Payload Fairing Scale Model Final Assembly

Figure 24 shows the fairing with a z-fold mechanical tuner, surrogate payload, payload adapter, and measurement probes added. The mechanical tuner is described in detail in Chapter four.



Figure 24: Space Availability within the Payload Fairing Scale Model

The fabrication method of composite fairing at OSU has one mechanical drawback. As fabricated, the Cu-Ni fabric is covered with a layer of resin and is not immediately exposed on the inside of the fairing cavity. This has little direct effect on the electrical properties the fairing since the resin acts as a low-loss dielectric. However, continuous electrical connection between to fairing half-

shells is needed to prevent leakage of the electromagnetic energy from the fairing, which lowers the cavity Q. The thin layer of resin on the fairing flanges was therefore carefully removed using fine-grit sandpaper to reveal the conducting fabric and allow a good electrical connection. A layer of conducting tape was then placed over the revealed fabric to ensure electric continuity in locations where the sanding may have damaged the conducting fabric.

CHAPTER IV

PAYLOAD FAIRING SUPPORTING ARTICLES

The fairing cavity has multiple internal supporting structures for different test applications. The mechanical stirrer or tuner is placed in the nose section of the fairing to redistribute electromagnetic energy within the cavity that results in formation of uniform reverberant field in the fairing model. The fabrication of the mechanical stirrer along with the description of an assembly to secure the stirrer is presented in section one of this chapter.

The payload in the fairing model is represented with a cylindrical aluminum shape. The payload is supported by a truss-like structure which acts as a payload adapter. Actual payload adapters used in the industry usually have a conical shape that usually separate the bottom volume from the rest of the cavity [14]. Section two explains the reasons for selecting a truss-like adapter and cylindrical payload.

Quality factor measurements of the fairing are conducted both by dual-ridge horn antennas, and specially designed, compact field probes. The field probe is designed to have minimum perturbation of reverberant electromagnetic fields within the fairing.

An electromagnetic shielding gasket is used on the flanges of the fairing to insure good electrical contact between the revealed conductive fabrics on the two half-shells, minimizing the leakage of energy. The gasket type and its installation are detailed in section four of this chapter. The chapter

Ends with a description of electromagnetic energy absorbing materials and acoustical absorbing foam which are widely used in launch vehicles fairing to protect the payload that affect the electromagnetic field levels that can be established within the fairing.

4-1 FAIRING MECHANICAL STIRRER

A mechanical tuner was designed to stir the electromagnetic energy within the fairing cavity, as described in Chapter 2. Shown in figure 25, it has a z-shaped or staircase design. It was cut from an aluminum sheet to minimize weight. The base length is 32 cm (15 in), and the top edge dimension is 10 cm (4 in). The width variation from the base to top is necessary to avoid contact with fairing wall when used in the nose section of the fairing, as shown in figure 24. A one meter long, quarter inch diameter, steel all-thread rod supports the tuner, which is suspended from the fairing top. The rod is all-thread to keep the z-fold half millimeter thick aluminum sheet fixed.



Figure 25: Mechanical Stirrer Used in the Payload Fairing Scale Model

The dimensions of tuner are given in figure 26.

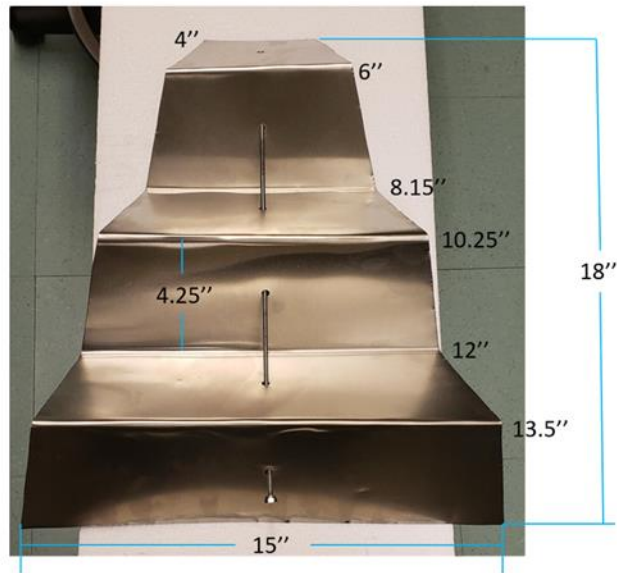


Figure 26: Fairing tuner dimensions in inches.

Figure 27 is a rough sketch of the tuner placement within the conical section of the fairing, drawn to scale.

The tuner is placed slightly off the central axis of the fairing model. There are both mechanical and electrical reasons for this placement. Mechanically, placing the tuner at the center of the fairing would prevent the two half shells from being sealed at the flanges. The electrical concern is the symmetry of fields. A center tuner simply rotates the electromagnetic modes that can be established in a circular-cylindrical cavity, so does not provide effective stirring. The tuner was therefore offset from the fairing centerline by 2.5 cm.

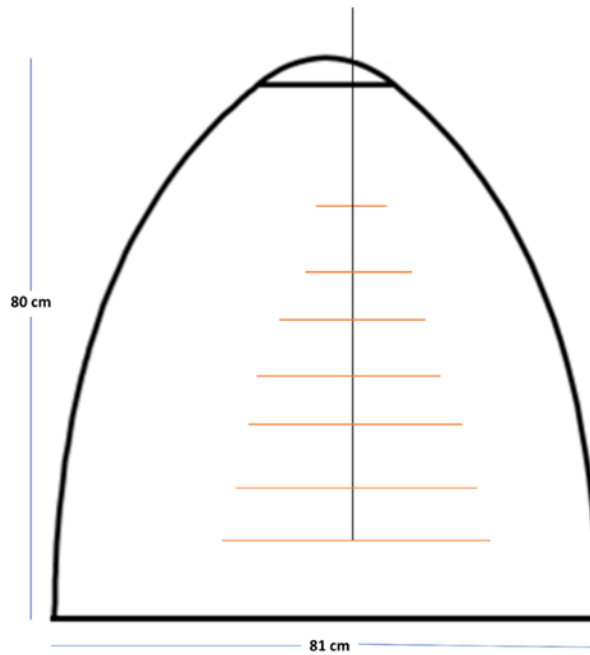


Figure 27: Sketch of the Tuner Placement Drawn to Scale

The all-thread steel rod supporting the tuner is one quarter inch in diameter. The fairing body at the top of nose section was drilled slightly larger than a quarter inch to both pass the rod and allow for its frictionless rotation. The vertical suspension of the tuner helps provide stability. Quarter inch steel, rather than aluminum, all-thread rod was selected to give greater strength and rigidity at the cost of slightly higher losses due to the lower conductivity.

The placement of the tuner inside the fairing model increases the conductive surface area within the fairing cavity. It does not significantly change the free space volume of the fairing cavity since it is only a half millimeter thick aluminum sheeting. The tuner can therefore be expected to lower the Q of the cavity slightly. However, the aluminum sheeting is highly conducting, and the Q reduction is insignificant.

Figure 28 shows the sketch of the design for final placement of the tuner in the fairing cavity model. The all-thread rod of the tuner extends to the middle cavity of the fairing and passes into the payload surrogate model. A quarter-inch hole was drilled in the top of the payload model to provide clearance for the all-thread. This configuration eliminated vibration of the tuner after it was stepped to a new position.

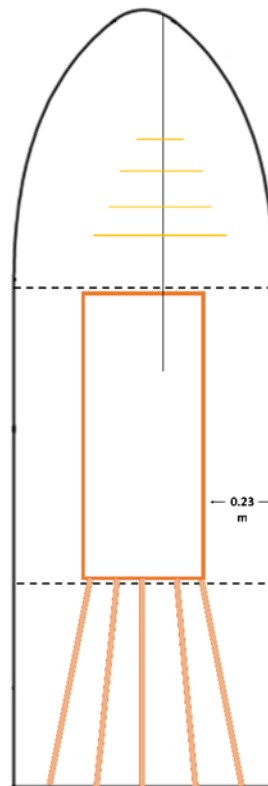


Figure 28: Rough Sketch of the Tuner Placement in the Fairing Cavity

Figure 29 shows the final placement of the mechanical stirrer in the conically rounded, nose section of the fairing scale model. Some of the aluminum edges of the tuner had irregularities, created during cutting of the aluminum sheet. It is not expected from such small protuberances to alter the fields configuration significantly. However, those edges were taped using conductive adhesive

aluminum tape for safety. The stirrer occupies significant space in the nose section but still leaves sufficient area for placement of measurement probes. A field probe consisting of a small dipole attached to a rigid coaxial cable can be observed on the left of the tuner in figure 29. The field probe will be described in later sections



Figure 29: Fairing Tuner Installed in the Top Cavity

4-1a Tuner Assembly

The z-fold tuner was rotated using the same stepper motor used previously in the scaled-avionics-box Q measurement tests in chapter three. The tuner rod is attached to the stepper motor by a 5 mm to 5 mm shaft coupler. Figure 30 shows the mechanical stirrer within the fairing coupled to the stepper motor outside of the fairing cavity.

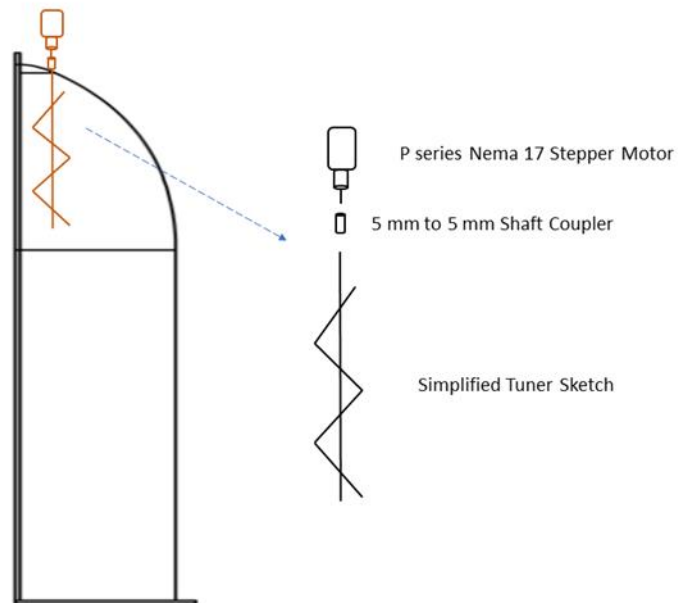


Figure 30: Tuner Assemble with the Stepper Motor

The motor used to rotate the stirrer is the P series Nema 17 [30] stepper motor. The specifications of the motor are listed in table 2. The 1.8 degrees step angle of the motor allows for 200 independent tuner positions with the fairing. However, it will be shown in chapter five that fewer number of stirrer positions are required to verify reverberation chamber operation within the payload fairing scale model.

P Series NEMA 17 Stepper Moto	
<i>Specification</i>	<i>Value</i>
Step angle	1.8 deg
Holding torque	72 Ncm
Rated current	2 A
Inductance	4.0 mH
Shaft diameter	5 mm
Shaft length	24 mm
Weight	500 g

Table 2: Nema 17 Stepper Motor Specifications

The Nema 17 motor provides enough torque to rotate the tuner structure but is sufficiently light (0.5 kg) that it may be placed on the fairing nose without stressing the thin fiberglass structure.

The stepper motor was mounted directly to the fairing flanges. The mounting apparatus is shown in figure 31. The flanges of the two fairing half shells stretch out 7.5 cm from the surface of the fairing wall. Two holes, each a quarter inch diameter, were drilled in the ceiling flanges of the fairing halves. A plain wooden block was bolted to the flanges, and then the stepper motor was secured to the wooden block by fastening the small screws of the NEMA 17 motor mount into the wooden block. Once the motor was fixed, the tuner rod was secured by the shaft coupler of the stepper motor. The simple tuner assembly structure along with the weight of the steel rod gives stable tuner rotation when the motor applies its 72 Ncm torque.

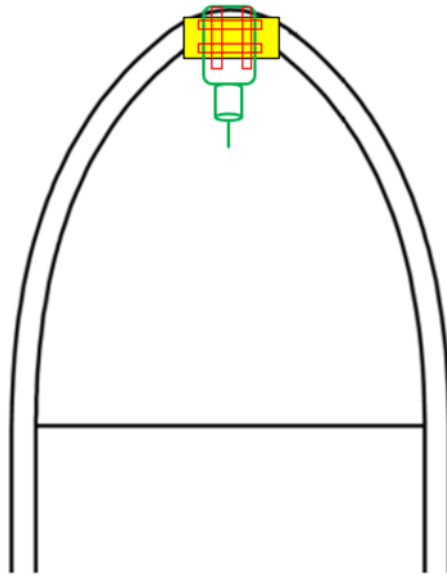


Figure 31: Rough Sketch of the Tuner Assembly

The actual assembly of the mechanical stirrer support apparatus in payload fairing scale model is shown in figure 32.



Figure 32: Actual Tuner Assembly Built for the Mechanical Stirrer of the Payload Fairing

4-2 PAYLOAD AND PAYLOAD ADAPTER

The surrogate payload scale model is represented by a hollow aluminum cylinder. The cylinder is 0.9-meter-high with a 0.41-meter diameter. It was fabricated by folding a sheet of flexible aluminum to form the cylindrical body. Then, two circular aluminum sheets were cut to cover the top and bottom faces of the cylinder. The seams of the structure, and anywhere the sheets overlapped, were sealed by conductive adhesive aluminum tape. Figure 33 shows the fabricated cylindrical payload model. The vertically aligned irregular bumps on the cylinder body visible in the figure is overlap of the aluminum sheet making the cylinder. The bumps are rivets used to fasten the overlap. Rivets are also used to join the sheets covering the top and bottom faces of the cylinder. The payload model has an all-around smooth surface, except for the overlaps of the sheets held fastened by rivets.



Figure 33: Cylindrical Payload Model

The statistical power balance model [18] requires the local regions of the fairing to be of approximately equal volumes. The power balance model is not the subject of analysis in this study. However, figure 34 is drawn to scale and shows that the three fairing regions have similar volumes.

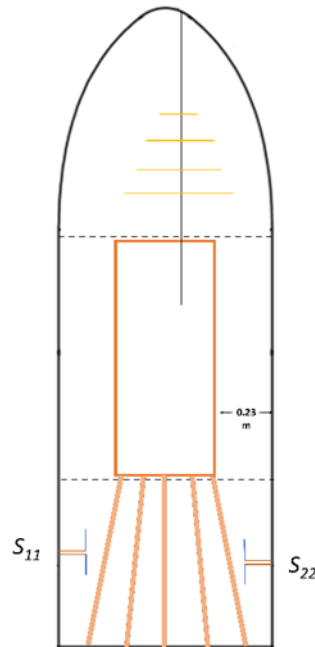


Figure 34: Fairing Local Regions

Figure 35 gives the dimensions of the OSU payload fairing scale model. The payload model's 0.41-meter diameter leaves 23 cm linear distance between the fairing wall and payload. This distance is sufficient for placement of the field probes and acoustic and RF absorbing foams and blankets in the middle cavity.

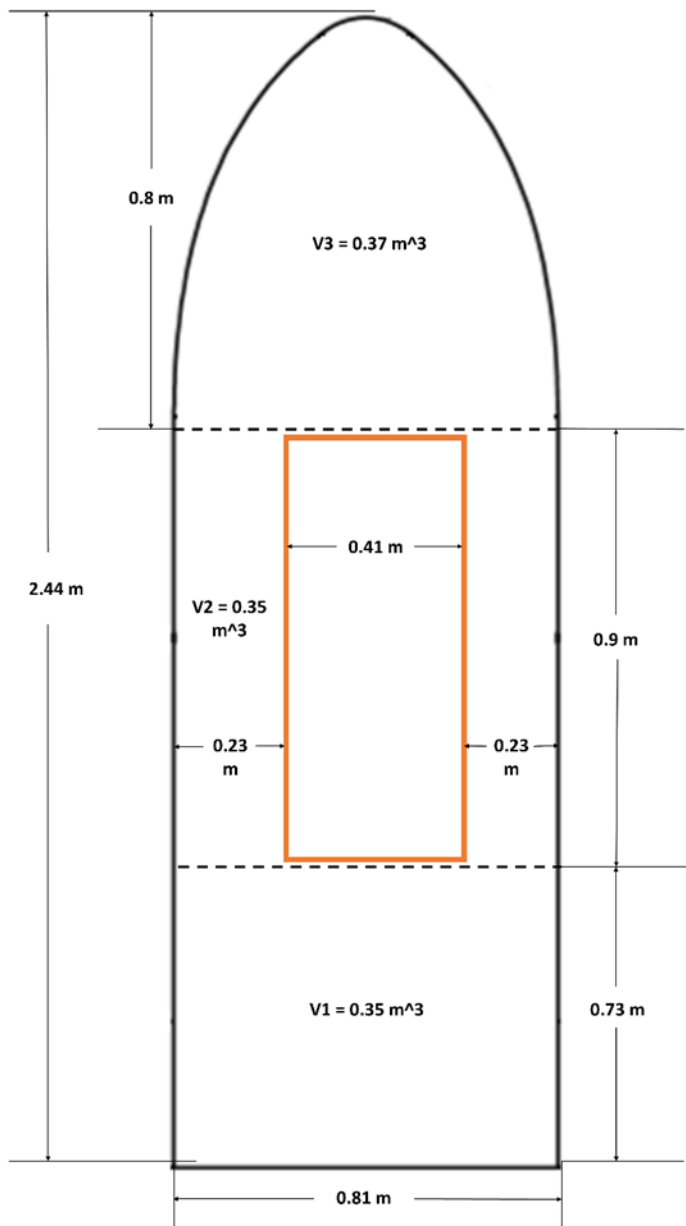


Figure 35: Payload Fairing Scale Model Dimensions

4-2a PAYLOAD ADAPTER

The payload adapter used for this study models a truss-type adapter [14]. It consists of five metallic struts attached to a circular baseplate. The struts were formed from multiple strips of thin aluminum that were cut to the proper height and width and bonded together. The struts were further strengthened with aluminum all-thread rods to provide rigidity when the payload is attached to the fairing base. Effort was placed to get a rigid structure and high conductivity with aluminum components for the measurements.



Figure 36: Final Assembly of the Payload and Payload Adapter Models

4-3 FIELD PROBE

The quality factor of the fairing is calculated from the S-parameters measured within the fairing. Dual ridge horn antennas have broadband response which make them a favorable choice for use in reverberation chambers and other cavities. The initial measurements of the composite payload fairing were conducted using A. H. Systems SAS 571 dual ridge horn antennas placed at the base of the fairing.

A smaller antenna probe was needed to perform measurements at various locations within the three regions of the fairing. Unbalanced dipoles of 5 cm and 10 cm were therefore fabricated by soldering two wire lengths to the center pin and shield of SMA male PCB panel edge mount connectors, as shown in figure 37. The longer probes are used to perform measurements from 1 GHz to 3 GHz and the shorter used at 3 GHz to 5 GHz.

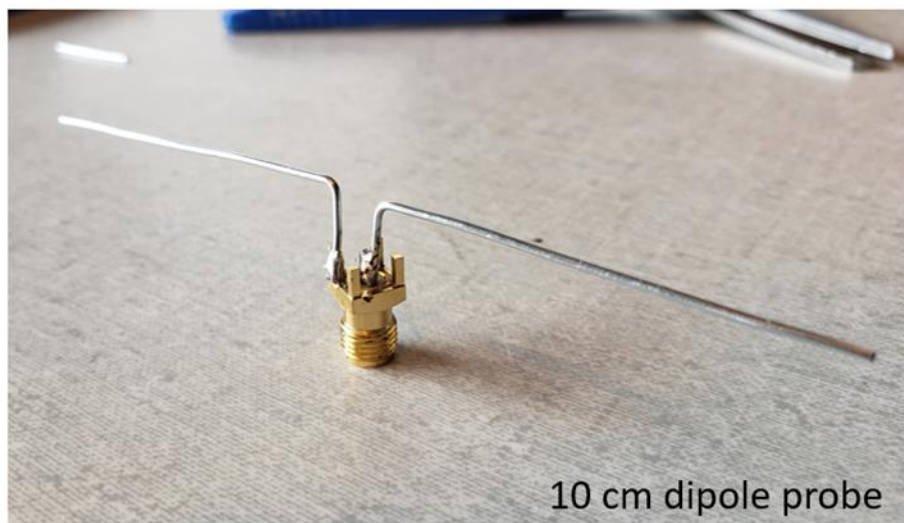


Figure 37: 5 cm and 10 cm Dipole Probes

4-3a FIELD PROBE ASSEMBLY

The measurement probes or antennas must be moved around the fairing cavity to collect data from multiple positions. Mechanical methods to move the probes would interfere with the tuner, payload struts, and absorbing materials. Instead, a field probe design that can be placed on the fairing wall

and access the inner cavity of the fairing through small drilled holes was selected to overcome the measurement challenge caused by limited fairing space. Figure 38 shows a diagram of the various components used to build the probe. The central component is a 10 cm SMA male to SMA female bulkhead rigid coax cable. The 5 cm and 10 cm dipoles built with SMA male edge mounts are connected to the SMA female side of the rigid coax without the bulkhead.



Figure 38: Field Probe Assembly Components

The coax end with the SMA female bulkhead is connected to a SMA male to N-type female adapter which connects the VNA cable to the field probe assembly. Figure 39 shows the 10 cm rigid coax manufactured by Pasternack Inc used in building the field probe. The bulkhead side is used to secure the rigid coax to the fairing body.



Figure 39: 10 cm Rigid Coax Cable from *PASTERNAK*

If multiple probes (rigid coax and dipole) are placed around the fairing body at different locations, the probes that are not being used for measurement must be shorted at the far end to prevent from leaking the energy out of the fairing cavity. An SMA male coaxial short from Centric RF is attached to the SMA female bulkhead end of coaxes when not used for measurement. Figure 40 shows a single field probe placed at the fairing.

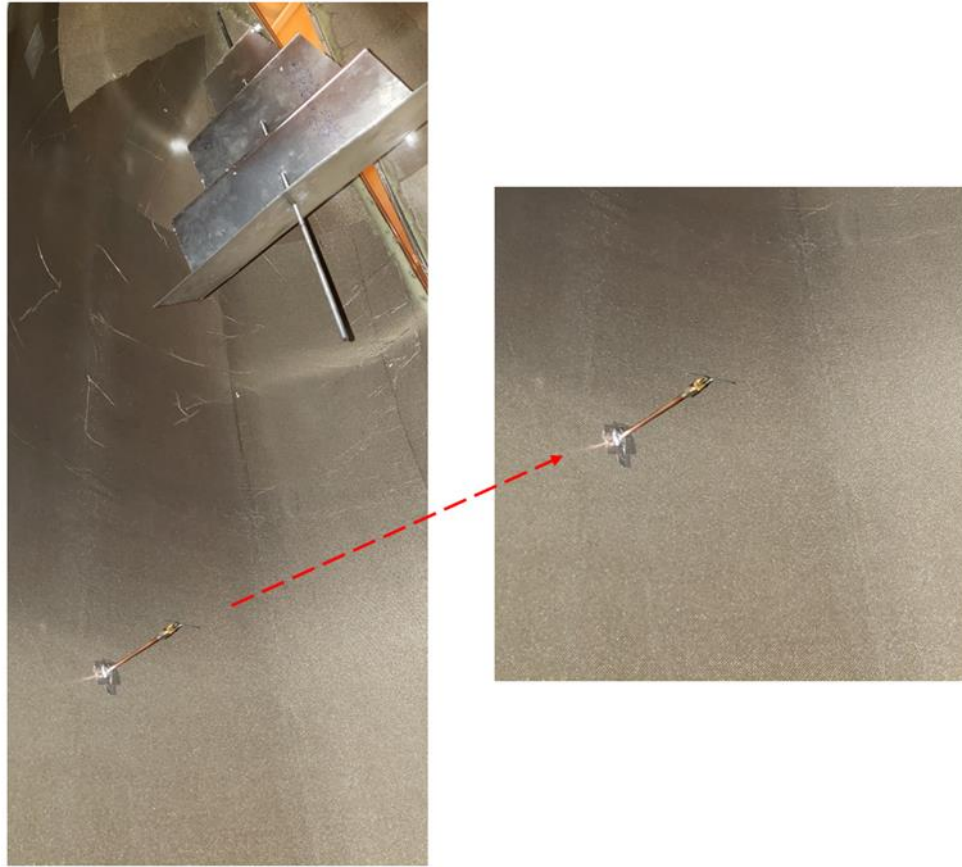


Figure 40: Field Probe Placement on the Fairing Wall

Table 3 lists the components used for assembling the field probes. The prices are reported as of February 2020 from the manufacturer of RFs.

Product	Manufacturer	Unit	Price	Total	Link
SMA Male to SMA Female Bulkhead Cable Using RG402 Coax, PE3C2892	Pasternack	13	\$ 47.50	\$ 617.5	https://www.pasternack.com/showProduct.aspx?SEName=sma-male-sma-female-rg402u-cable-assembly-pe3c2892&ProductID=
SMA Female Connector Solder Attachment Thru Hole PCB, PE4117	Pasternack	13	\$ 14.39	\$ 187.07	https://www.pasternack.com/sma-female-standard-thru-hole-pcb-connector-pe4117-p.aspx
C4851 SMA/Male Coaxial Short 18 GHz	CentricRF	13	\$ 15.52	\$ 201.76	https://www.centricrf.com/shorts/c4851-sma-male-short/
			Grand Total	\$ 1006.33	One Thousand and Seven Dollars

Table 3: Field Probe Assembly Components Summary

4-4 ELECTROMAGNETIC SHIELDING GASKETS

Electromagnetic shielding gaskets must be used around the flanges of the fairing to provide a continuously conductive surface inside the fairing. A crushable fabric over foam EMI gasket, the Tech-Etch Industries 2400 Series Metalized fabric over foam gasket listed in figure 41 and sketched in figure 42, was selected. When closing the two fairing halves, the gaskets are crushed, and the exposed conductive fabric establishes a continuous electrically conductive surface between the two fairing halves.

- 2400 Series Metalized Fabric Gasket (Fabric over Foam)
 - Mounted by double sided tape (3M 9495LE non-conductive adhesive)
 - Max width = 1”
 - Max thickness = .375”

Figure 41: EM Shielding Gasket Types from *Tech-Etch*

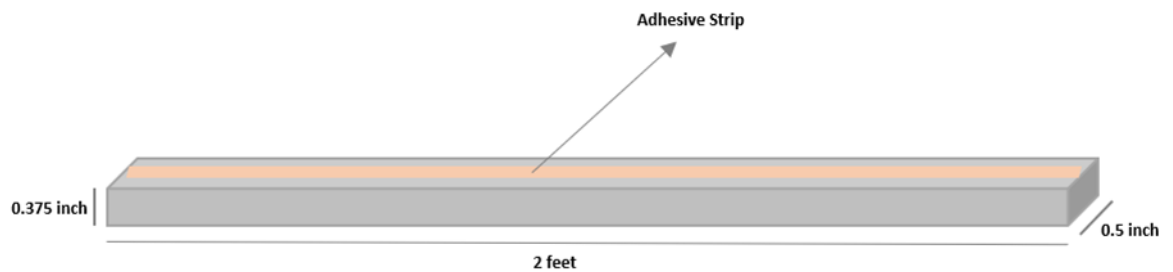


Figure 42: Tech-Etch 2400 Series Fabric Over Foam Gasket

The gaskets were installed on one of the fairing halves, as shown in figures 43 and 44. The gasket is applied to the conducting tape placed over the conducting fabric exposed by sanding the resin, as discussed in the previous chapter. It is crushed against the conducting tape on the other fairing half when closed, giving full electrical continuity and providing shielding.



Figure 43: Gaskets Installed on the Fairing Flange



Figure 44: Single Layer of Conductive Adhesive Aluminum Tape for Gasket Conductivity

4.5 ACOUSTIC AND RF ABSORBING FOAMS

Acoustical absorber foams to be used within the scale model fairing in this study to model the environment within the fairing are identified. Melamine foams have been recommended by a NASA technical report [15] for acoustic attenuation during launch. Acoustical absorber foams from Acoustical Surface Inc. were ordered and installed on the middle cavity fairing wall, surrounding the spacecraft model. The installation of the foams is described in the next chapter where quality factor values are measured for the local cavities of the fairing. Table 4 summarizes some general specifications of the acoustic foam (BASF Basotect-G Melamine).

Acoustical Absorbing Foam	
Manufacturer	Acoustical Surface Inc.
Material	Open cell melamine foam
Thickness	1 inch
Density	9 Kg/m ³
Panel size	2' x 2'
Features	Designed for sound absorption in a wide range of frequencies

Table 4: Acoustic Absorber Foam (BASF Melamine)

In actual payload fairings in the industry, RF absorbing materials are also used within fairings to suppress electromagnetic interference near the payload. RF absorbing materials are selected according to studies conducted in a technical report by NASA [16] on predicting the RF field strength in conductive enclosures.

The RF absorbing foam selected is a metal loaded foam sheet manufactured by MAST Technologies (MF11-0002-00). It has broadband operation and is one-half inch thick, sufficiently thin to allow clearance for the field-probe assemblies. Table 5 summarizes the specifications of the

RF absorbing foam used in the payload fairing scale model. The foam absorber is installed on the fairing walls in the payload region.

RF Absorbing Foam	
Manufacture	Mast Technologies
Material	Conductive carbon loaded sheet
Frequency Range	1 GHz – 18 GHz
Thickness	0.5"
Sheet Size	24" x 24"

Table 5: RF Absorbing Foam (MF11-0002-00)

The second absorbing materials used are the RF absorbing sheets that are installed on the payload itself. They are also manufactured by MAST Technologies (MR21-0001-01). The RF sheets are broadband, effective from 1 GHz to 20 GHz. The sheets are half millimeters thick and come with pressure-sensitive adhesive (PSA) backing. Their installation on the spacecraft model is shown in the local cavity measurement, section 5.8.

RF Absorbing Sheet	
Manufacture	Mast Technologies
Material	Thin magnetically loaded sheet
Frequency Range	1 GHz – 20 GHz
Thickness	0.02" (0.5 mm)
Sheet Size	24" x 24"

Table 6: MR21-0001-01

CHAPTER V

QUALITY FACTOR MEASUREMENT RESULTS

The time-domain method used to measure the quality factor of a cavity is validated in the Oklahoma State University ETS-Lindgren SMART-80 reverberation chamber. The SMART-80 measurements will be followed by the measurement of the payload fairing Q both in the time-domain and frequency domain. The limitations of the frequency-domain quality factor method and antenna-efficiency corrections needed are reviewed. The Q of the payload fairing is also measured in the time domain using a single antenna to explore the feasibility of this method.

The effect of placing a lossy object within the fairing is measured. The effects of the payload and payload adapter models on the Q is discussed in section 6 of the chapter. The characteristics of the dipole field probes are discussed in section 7. The chapter ends with local cavity measurements of the Q using the field probe after adding the absorbers to the middle cavity.

5_1) ETS-LINDGREN SMART-80 REVERBERATION CHAMBER

The SMART-80 reverberation chamber is a rectangular cavity made of Zinc coated galvanized steel walls [18]. Table 5.1 lists the dimensions and specification of the reverberation chamber at Oklahoma State University Robust Electromagnetic Field Testing and Simulation Laboratory [17].

Length	13.41 m
Width	6.09 m
Height	4.87 m
Surface Area	345 m ²
Volume	398 m ³
Frequency Range	80 MHz - 18 GHz

Table 7: ETS-Lindgren SMART-80 Chamber Specifications

Time-domain quality factor measurement of the SMART-80 and any other reverberant cavity can be performed using the energy decay rate method described by Richardson [3]. One technique to get the energy decay is measuring the S21 parameter between two antennas within the cavity in the frequency domain and performing an inverse fast Fourier transform (IFFT) to yield the time-response. To measure the S-parameters in SMART-80, two dual-ridge horn antennas were used. The horn antennas had a frequency range of 700 MHz to 18 GHz and were manufactured by A.H. Systems. The VNA used to measure the S-parameters was a Keysight Technologies 8722ES (50 MHz - 40 GHz). A Keysight N type 50 Ohm calibration kit (85032F) with frequency range (DC to 9 GHz) was used to calibrate the coaxial cables between VNA and the horn antennas ports. The test setup is shown in Figure 45.

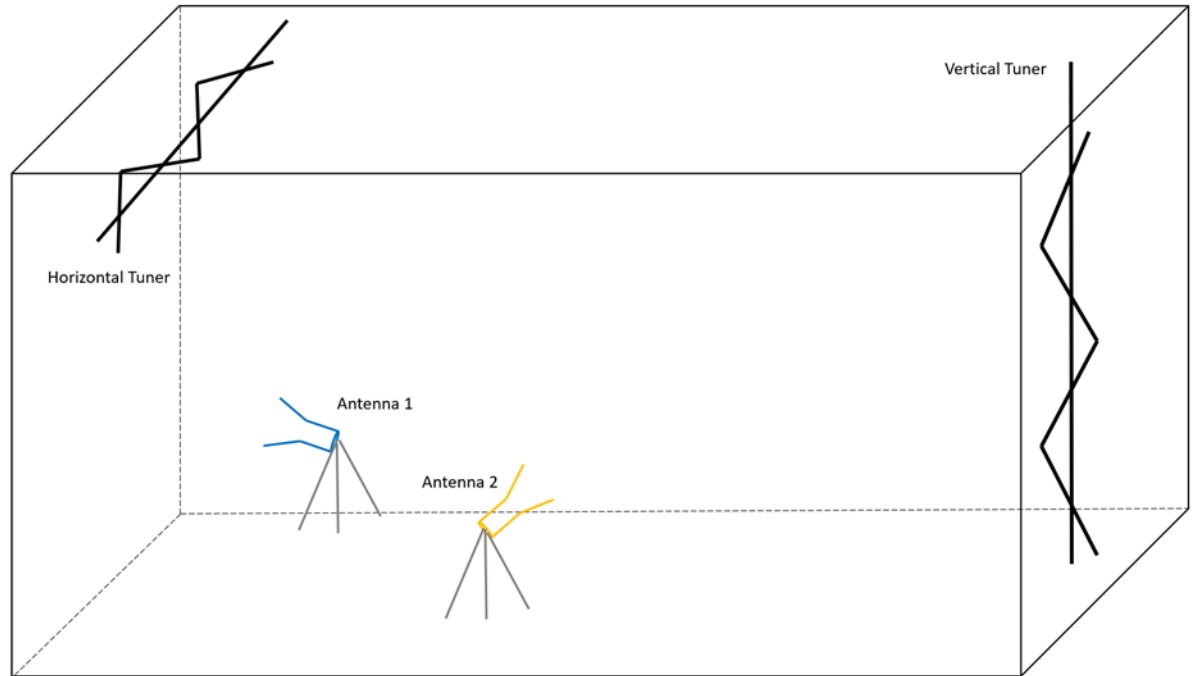


Figure 45: SMART-80 Chamber Quality Factor Measurement Setup

The continuous-wave (CW) S-parameters were measured at center frequencies over 100 MHz bandwidth centered 1, 2, 3, 4, 5, and 6 GHz. The VNA sweep time was set to 6 sec to allow sufficient time for the cavity field to stabilize. 1601 frequency samples, the maximum of the VNA in a single measurement, were sampled over the 100 MHz bandwidths to provide the highest resolution available in time-domain decay. The frequency domain measurements were repeated 70 times with the SMART-80 set to unique positions to provide unique, random realizations of the chamber field.

The measured S-parameters at each tuner position were converted to complex-amplitude and transformed from frequency-domain to time-domain using the inverse fast Fourier transform (IFFT) routine in MATLAB. The steps taken are detailed in Appendix A. The magnitude-squared time-domain response was then averaged over the 70 tuner steps and converted to decibels to yield the time-decay profile of the chamber field. An example is shown in figure 46.

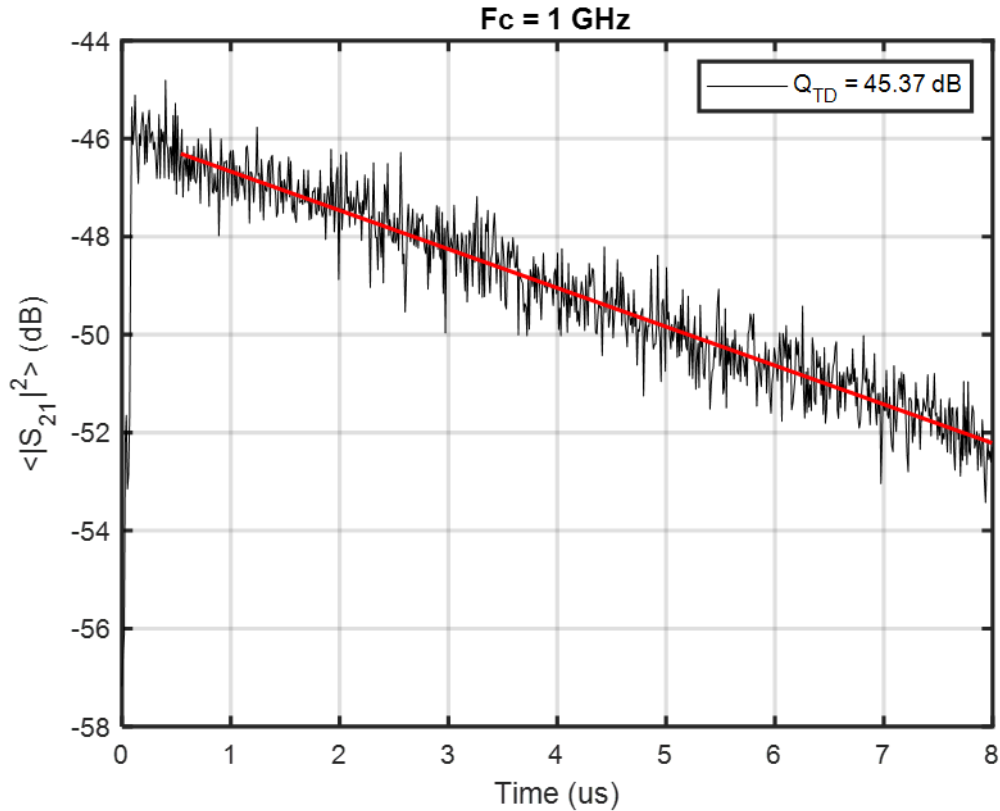


Figure 46: SMART-80 Time-Domain Q at 1 GHz with 70 Tuner Positions

The slope of the decay is used to find the chamber quality factor. The red line in the figure shows a linear fit to the energy decay, whose slope D in dB/us is used to find the time-constant and quality factor of the chamber using equations (2.15) and (2.14), respectively.

As discussed in chapter two, the advantage of time-domain quality factor measurement is that the power decay of the chamber is not affected by the antennas or probes efficiencies. The energy decay in figure 46 gives a measured SMART-80 quality factor of 45.37 dB at 1 GHz. An interesting observation is the distinction between the pre-reverberant and reverberant phases of the chamber as predicted by the reverberation theory. The pre-reverberant phase of the SMART-80 chamber at 1 GHz lasts around a half microsecond before the reverberant environment is established and the power loss begins through the various mechanism such as the chamber wall losses.

The measured power decay curves and associated quality factors for the SMART80 from 1 GHz to 6 GHz are shown in figure 47. The Q increases with increasing frequency as expected. The pre-reverberant phase however stays at about the same duration of a half microsecond for the six cases. The level of power decreases with higher frequency, which is also expected as the wavelengths gets shorter. The seventy tuner positions provide sufficient independent samples to achieve the statistical uniform electromagnetic fields within the reverberation chamber.

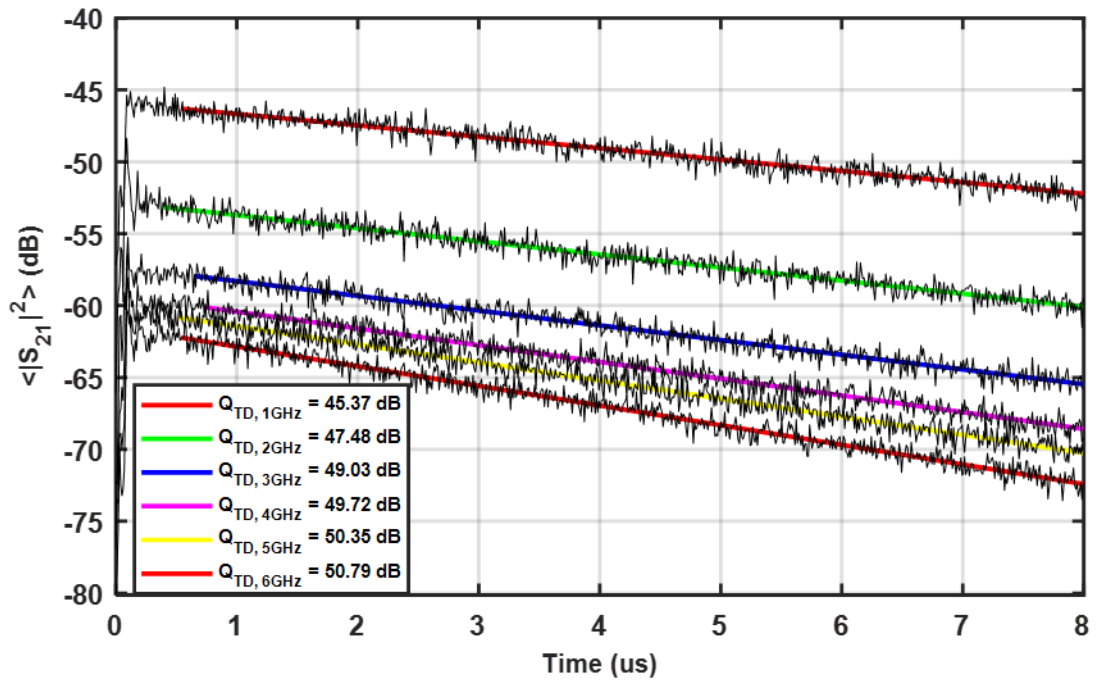


Figure 47: Power Decay Profiles for SMART-80 Chamber

5_2) Payload Fairing Quality Factor

The same method of determining the time-domain quality factor of the SMART-80 reverberation chamber was used to characterize the quality factor of the payload fairing. The same test equipment, including the VNA, coaxial cables, and the dual-ridge horn antennas, was used. The z-fold tuner in the nose of the fairing cavity was rotated to yield independent field samples. The quality factor of the fairing cavity was measured using a 100 MHz bandwidth centered at 1 to 6 GHz.

The quality factor is initially measured with the fairing only containing the two dual-ridge horn antennas. The antennas are sitting at the base of the fairing pointing upward at the tuner, as shown in figure 48. The measured time-decay profile centered at 1 GHz and averaged over 18 tuner positions is shown in figure 49.

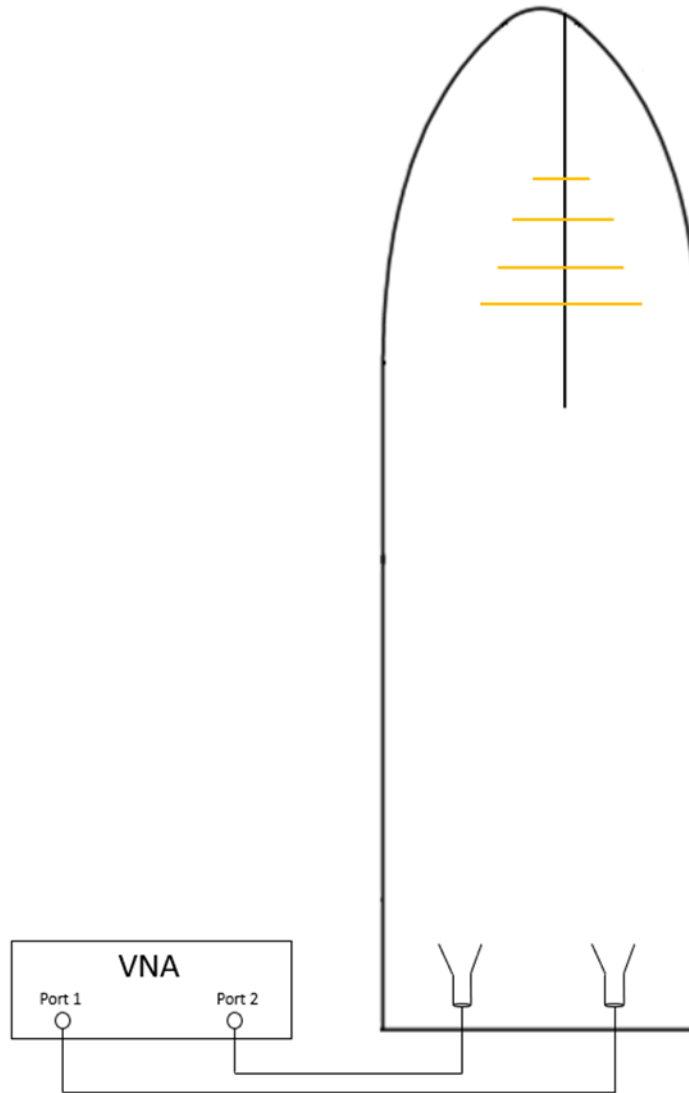


Figure 48: Measurement Setup for Time-Domain Quality Factor Measurement of Empty Payload Fairing

The rate of the decay is significantly larger than the SMART-80 reverberation chamber as the fairing model is much smaller and the walls are less conducting. The pre-reverberant phase is also shorter, lasting around 0.2 microseconds. The quality factor determined by the decay rates is slightly over 32 dB.

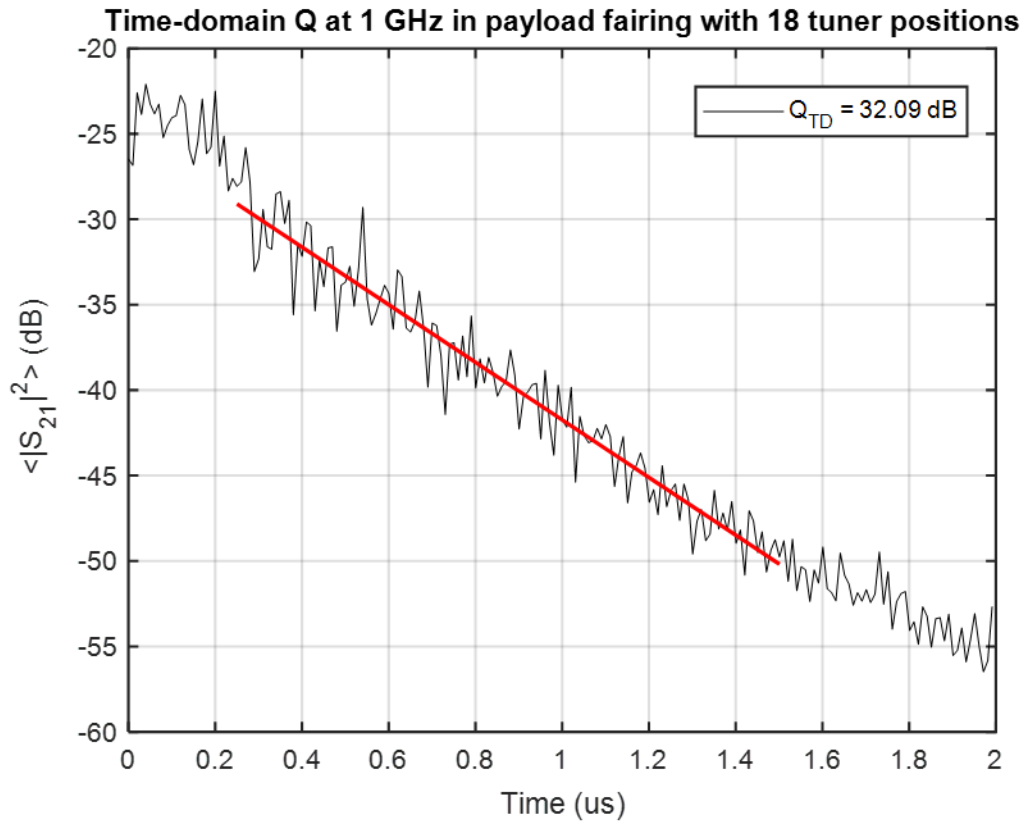


Figure 49: Empty Fairing Q at 1 GHz using 18 tuner positions

Power decay profile curves for the empty fairing centered at 1 GHz through 6 GHz are shown in figure 50. The quality factor values are summarized in table 8. The Q ranges from 32.1 dB at 1 GHz to 41.1 at 6 GHz.

Frequency (GHz)	Q_{TD} dB
1	32.09
2	34.31
3	36.91
4	39.94
5	40.09
6	41.10

Table 8: Summary of Q_{TD} Measurements of Empty Payload Fairing Cavity

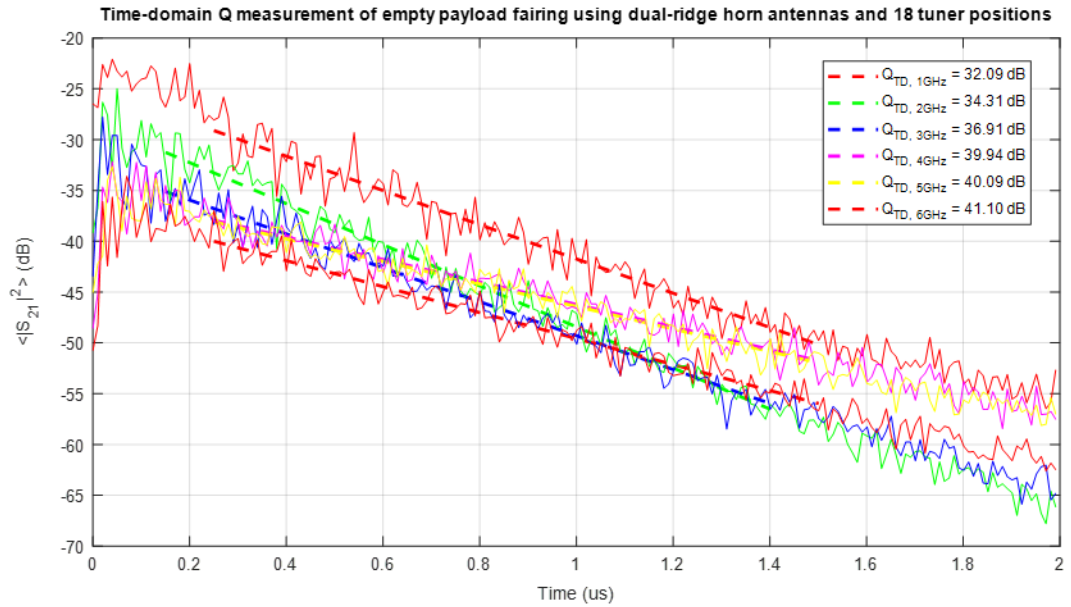


Figure 50: Empty Payload Fairing Cavity Power Decay Profile

5_3) QUALITY FACTOR IN FREQUENCY-DOMAIN

The frequency-domain calculation of the SMART-80 and payload fairing cavities using the approach of Hill reviewed in Chapter 2 is now considered. As noted, the measurement of antenna efficiencies affects the frequency-domain Q measurements. The dual-ridge horn radiation efficiencies are assumed to be small [12]. As will be shown, however, the radiation efficiencies of the fabricated measurement probes must be considered. Impedance mismatch efficiencies of both the dual-ridge horns and the measurement probes must be compensated.

5_3a) REFLECTION COEFFICIENT IN REVERBERATION CHAMBER

The antenna mismatch efficiency is determined by the free-space reflection at the antenna input. The free-space reflection can be found in a reverberant environment such as the SMART-80 or the payload fairing by coherently averaging the measured reflection over independent positions of the tuner. The random reflected energy from the cavity averages to zero while the constant free-space reflection coherently adds. The reflection coefficient and efficiency of the dual-ridge horn antennas were measured both in the SMART-80 chamber and payload fairing.

Figure 51 shows that the free-space reflection coefficient of the dual-ridge horn antennas measured in the SMART-80 chamber and an anechoic chamber. The SMART-80 reflection was averaged over 200 tuner positions. Good agreement is achieved overall. The discrepancy above 4 GHz is due to imperfect calibration of the long cables that were used in the reverberation chamber.

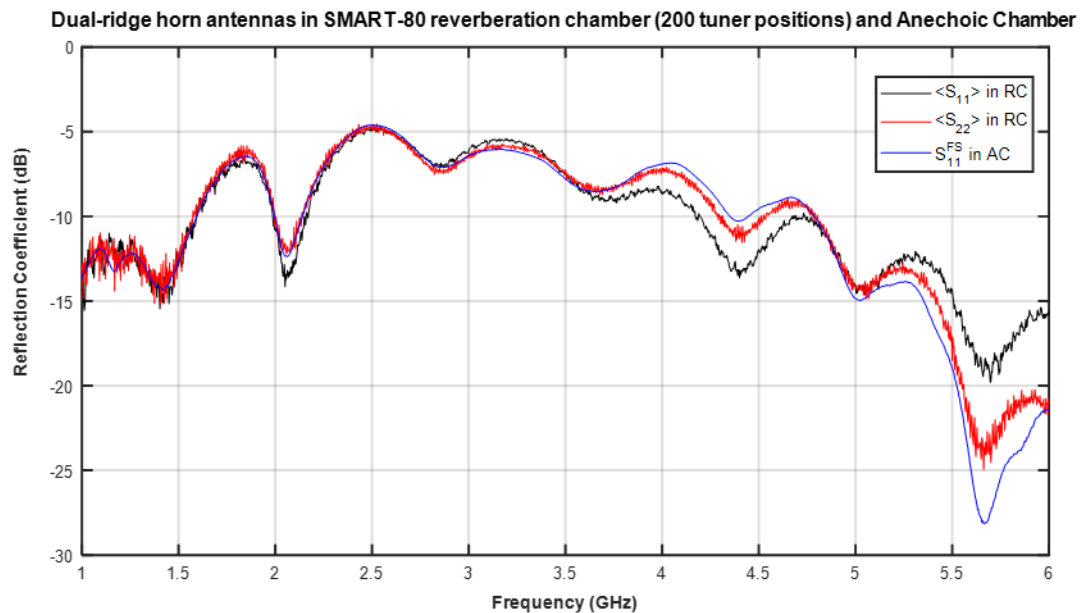


Figure 51: Reflection Coefficient of the Dual-Ridge Horn Antenna in Reverberation and Anechoic Chambers

The reflection coefficient of the horn antennas was also measured within the payload fairing cavity. As seen in figure 52, The fairing tuner was less effective than the SMART-80 tuners and averaging over 100 tuner positions did not sufficiently remove the random reflections. Therefore, a moving average over a 150 MHz bandwidth was applied, a process known as “frequency stirring” [5]. The result is shown in figure 53. Good agreement with the anechoic measurements is achieved with frequency stirring added. Reverberant fields are therefore established within the fairing and reverberation chamber operation is achieved using averaging over tuner positions and frequency.

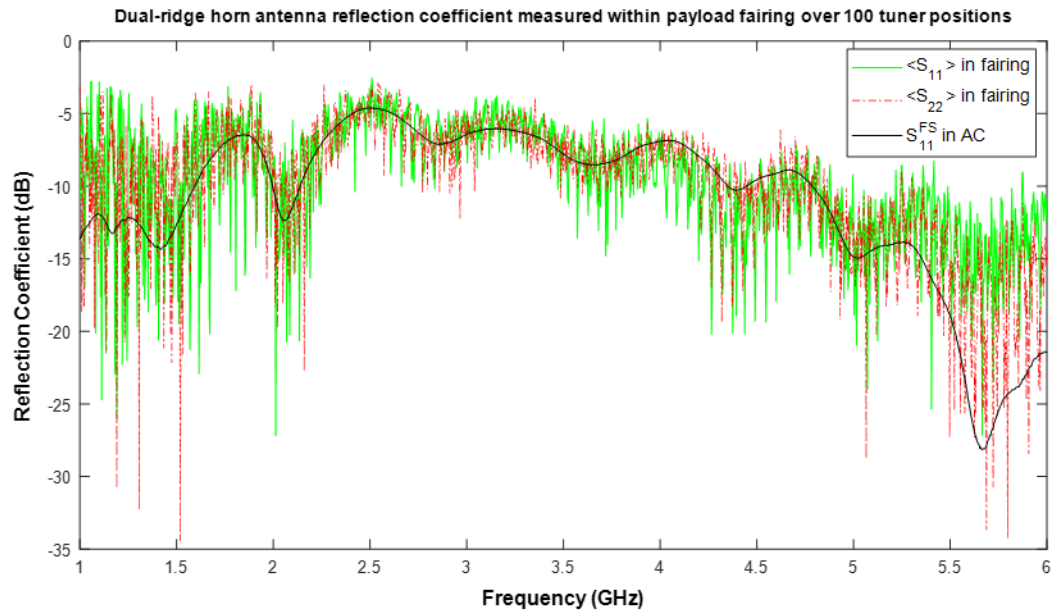


Figure 52: Reverberation Chamber Reflection Coefficient of Horn Antennas

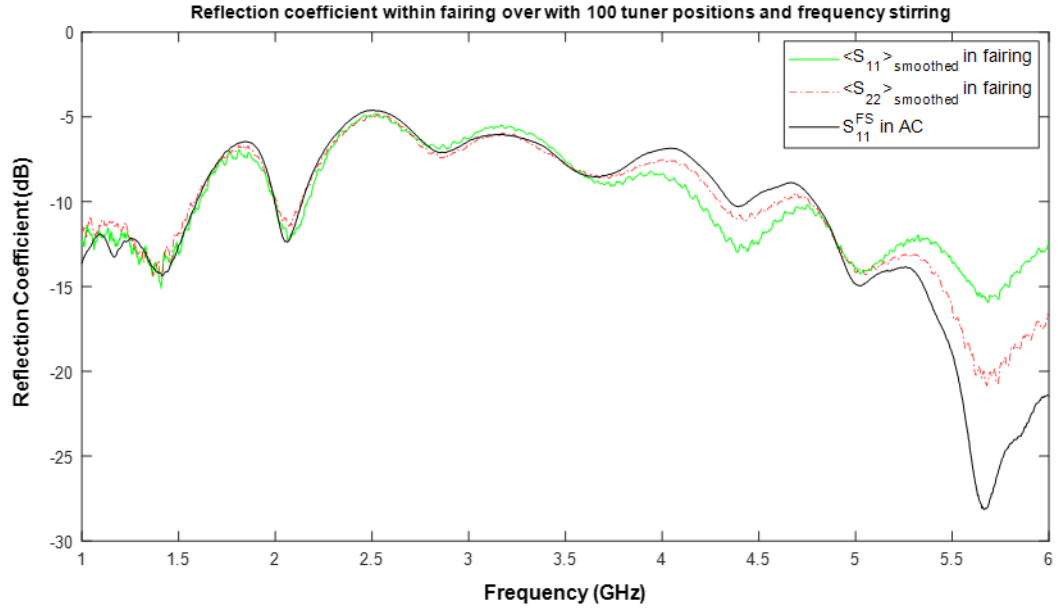


Figure 53: Antenna Reflection Coefficient Measurement in Payload Fairing

5_3b) ANTENNA EFFICIENCY

If dielectric and conductive losses of the antenna are negligible, then the efficiency of the antenna is determined solely by the impedance mismatch [12]:

$$\eta_1 = 1 - |S_{11}^{\text{FS}}|^2, \quad \eta_2 = 1 - |S_{22}^{\text{FS}}|^2, \quad (5.2)$$

where η_1 and η_2 are the transmitting and receiving antennas efficiency. The antenna efficiency found using the reverberation chamber reflection coefficient measurement is

$$\eta_1 = 1 - |\langle S_{11} \rangle|^2, \quad \eta_2 = 1 - |\langle S_{22} \rangle|^2, \quad (5.3)$$

where $\langle \rangle$ indicates averaging over tuner positions and/or frequency. The dual-ridge horn antenna match efficiencies as found from both the anechoic chamber and the SMART-80 reverberation chamber measurements are plotted in figure 54.

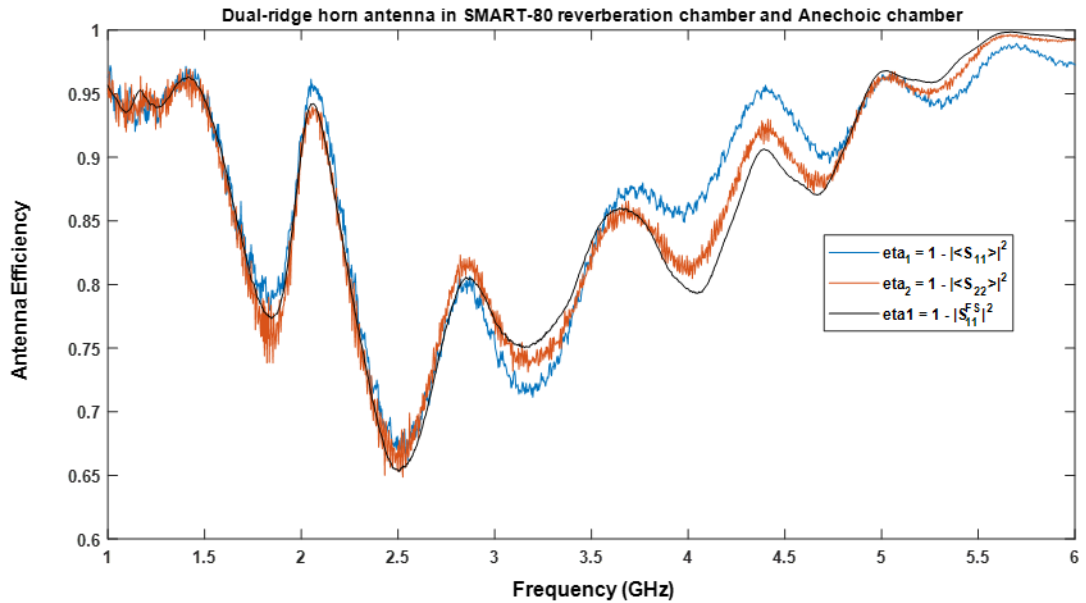


Figure 54: Dual-Ridge Horn Antenna Efficiency Measured in Reverberation and Anechoic Chambers

The dual-ridge horn pair that were used to measure the frequency-domain quality factor of the SMART-80 chamber were then placed within the empty fairing model. The mechanical tuner was rotated for 100 positions and the S-parameters of the two antennas were measured. The Q of the fairing cavity from 1 GHz to 6 GHz was then found from the measured S parameters. The same test setup as in time-domain Q measurement of the fairing in figure 48 was used. Figure 55 shows the match efficiency of the dual-ridge horn antenna measured within the payload fairing cavity. The ensemble average of the antenna reflection coefficient (S11), shown in blue has large variation and does not approximate the smooth reflection measured in the anechoic chamber, again indicating that the z-fold tuner alone is unable to adequately stir the reverberant field.

A 50-point, 150 MHz moving average frequency stirring of was applied to the reflection coefficient measurement of the horn antennas in payload fairing to get the smoothed match efficiency, shown in figure 55. It is considerably smoother and is in acceptable agreement with the match efficiency measured in the anechoic chamber, shown as the black trace. This test further demonstrates that the fairing cavity with both mechanical and frequency stirring behaves as an over-moded reverberation chamber.

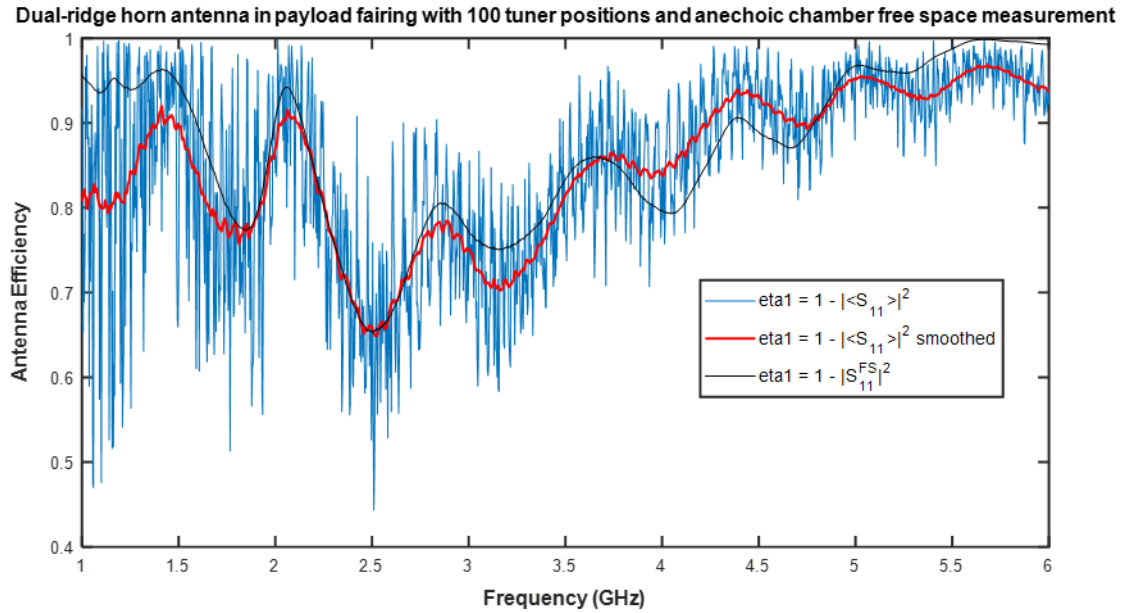


Figure 55: Horn Antenna Efficiency Measurement in Payload Fairing Compared to Free Space Measurement

5_3c) CORRECTION FACTOR

The correction factor for the frequency-domain Q measurement technique is determined by the mismatch efficiency of the antennas. Equation 2.13 from chapter two is repeated here to show the

use of correction factor to compensate for the impedance mismatch effects of the antennas in frequency-domain Q method:

$$Q_c = \frac{Q}{\eta_1 \eta_2}. \quad (5.4)$$

The correction factor is $\frac{1}{\eta_1 \eta_2}$. The correction factor for the horn antennas as measured in the SMART-80 reverberation chamber using 200 tuner positions is shown in figure 56. The correction is more than 2 dB at frequencies where the horn antennas were less well matched in figure 54 (1.75 GHz, 2.4 GHz, and 3.2 GHz), whereas at the band edge the correction is less than 0.5 dB. Above 5.5 GHz, the correction factor is significantly lower due to the good match that the antennas provide at that frequency.

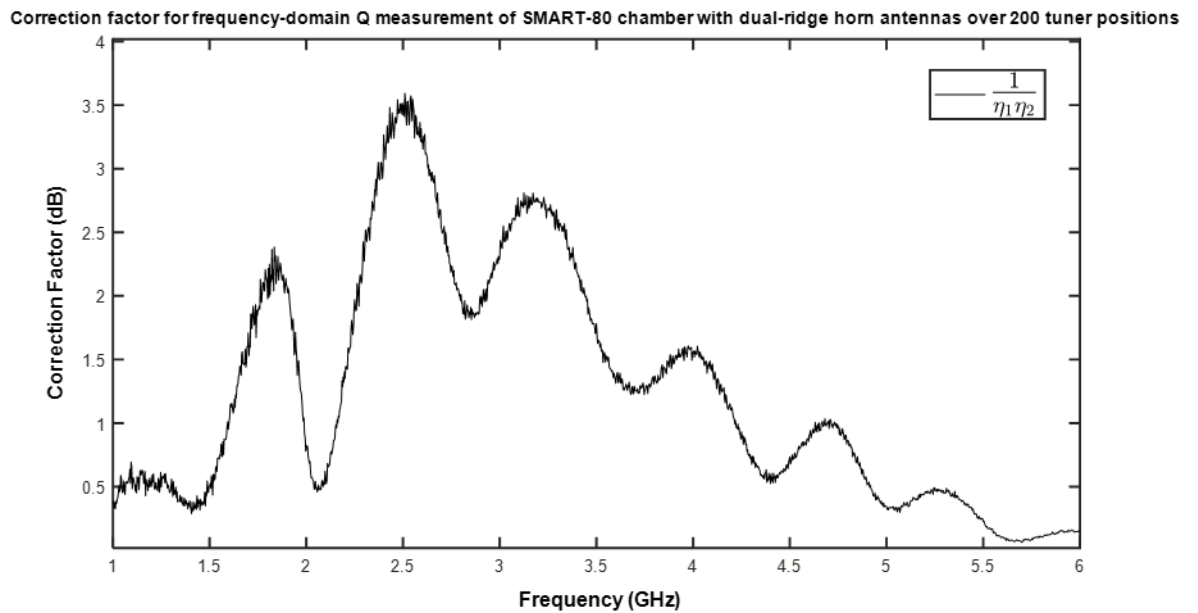


Figure 56: Dual-Ridge Horn Antenna Correction Factor Shown for the SMART-80 Chamber

The horn-antenna correction factor was also measured in the payload fairing. The plot in figure 57 shows the correction factor levels which will be applied to the quality factor measurement of the payload fairing in frequency-domain. The red trace when frequency stirring is added shows good agreement with figure 56, as expected.

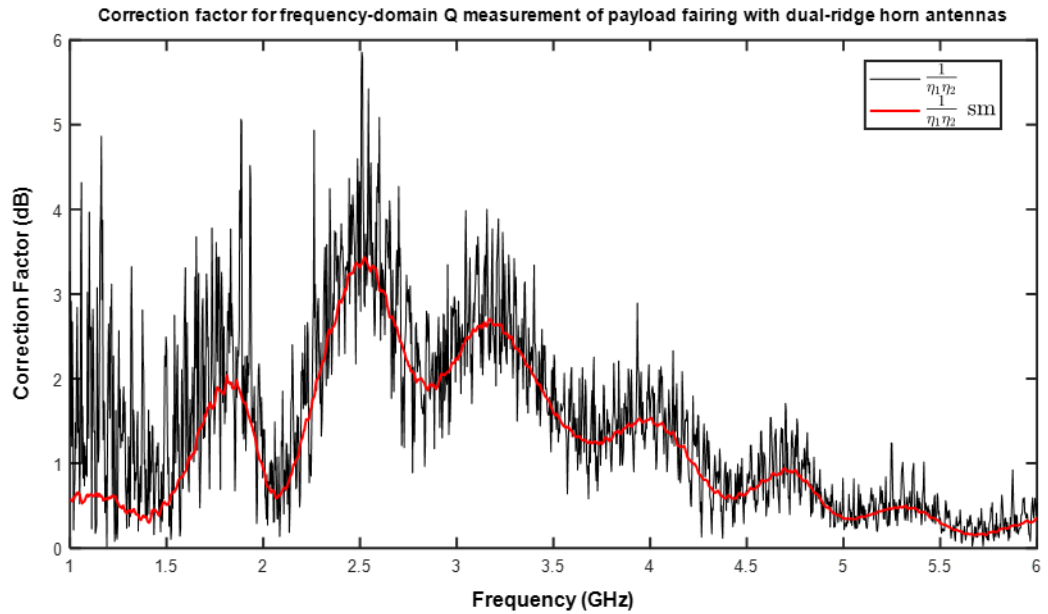


Figure 57: Dual-Ridge Horn Antenna Correction Factor for Payload Fairing Scale Model

5_3d) PAYLOAD FAIRING Q IN FREQUENCY-DOMAIN

The quality factor of the empty payload fairing measured in the frequency domain from 1 GHz to 6 GHz is shown in figure 58. The antenna mismatch correction factor was applied. An ensemble over 100 tuner positions but no averaging over frequency is shown in the black curve. The Q varies over 7 dB near single frequencies despite the large number of tuner positions used. The addition of 150 MHz bandwidth frequency stirring smooths the measured Q considerably.

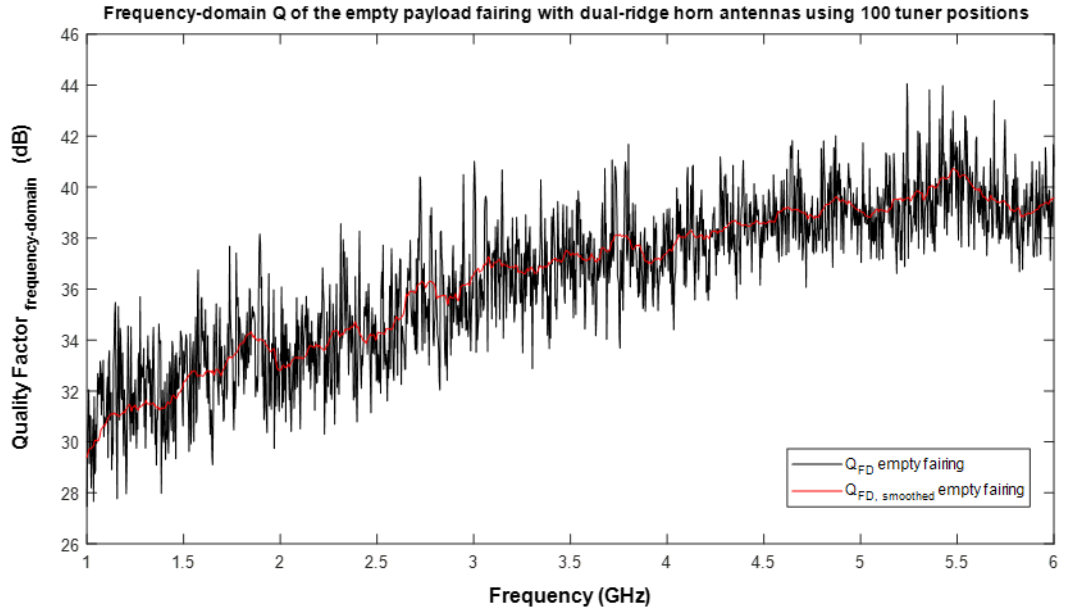


Figure 58: Frequency-Domain Quality Factor Measurement of Empty Fairing

The cavity quality factors measured in the time and frequency domains are measured in figure 59. The antenna power losses (dielectric and conductive) are not compensated in frequency domain Q measurements. This explains the relation between the time-domain and frequency-domain quality factor methods. The frequency-domain measured Q will therefore be reduced below that measured in the time-domain by the product of the antenna radiation efficiencies [20]. The time-domain Q is slightly higher than the frequency-domain Q at all frequencies, with the poorest agreement at 3 GHz. The time-domain measurement is accepted as the more accurate representation of the cavity quality factor, including antenna loading effects.

Frequency-domain Q of the empty payload fairing with dual-ridge horn antennas using 100 tuner positions compared with time-domain

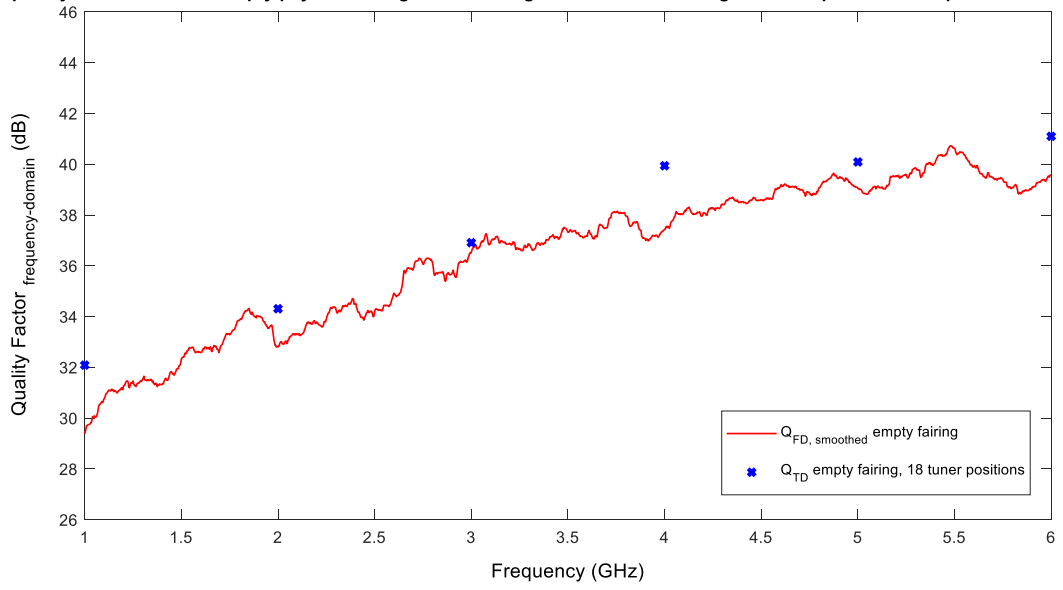


Figure 59: QFD Compared to QTD Values for Empty Fairing

5_4) PAYLOAD FAIRING Q WITH SINGLE ANTENNA

The Q of the empty payload fairing was measured in time-domain using a single dual-ridge horn antenna. The same bandwidth, center frequencies, frequency sampling, and measurement time as used in the two-antenna time-domain measurements was used here. The S-parameters for this test was measured for 40 tuner positions. The synthesized time-domain mean response with the fit linear-decay lines are shown in figure 60. The variations in the power decay curve are smaller than the two-antenna measurement presented earlier where only 18 tuner positions were used, giving better confidence in the decay fit line. The measured quality factors show good agreement with the earlier two-antenna tests.

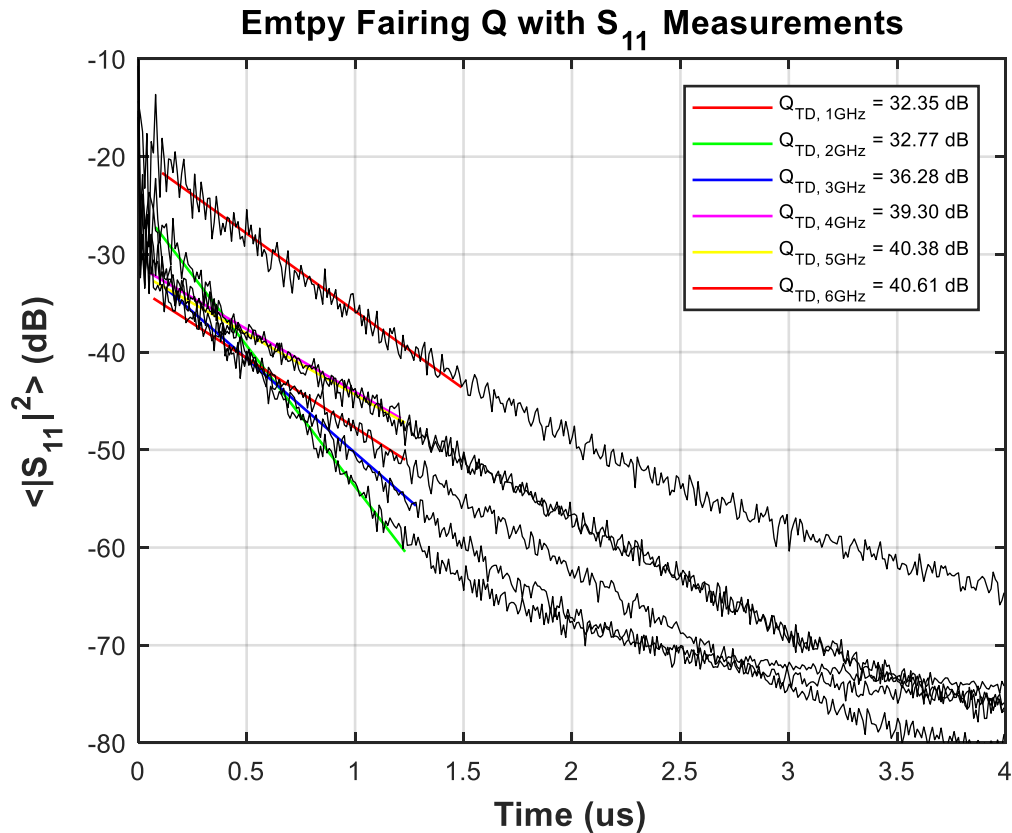


Figure 60: Single Antenna Power Decay Profile of Empty Payload Fairing

The two antenna and single antenna time-domain, and frequency-domain quality factor measurements are summarized in table 9. From 1 to 4 GHz, the Q increases by 2 dB with every 1 GHz frequency increase. From 4 to 6 GHz, it increases by 1 dB. The difference between the time and frequency methods is 2 dB, consistent with earlier observations. The antennas are not significantly loading the cavity because the single antenna measurements closely follow the two-antenna test. Therefore, other losses such as the fairing wall and apertures losses dominate.

Frequency (GHz)	$Q_{TD} (S_{21})$ dB	$Q_{FD} (S_{21})$ dB	$Q_{TD} (S_{11})$ dB
1	32.09	29.38	32.35
2	34.31	32.84	32.77
3	36.91	36.54	36.28
4	39.94	37.43	39.30
5	40.09	39.04	40.38
6	41.10	39.57	40.61

Table 9: Summary of Single Antenna (S_{11}) Q and Comparison with Two Antenna (S_{21}) Measurements

5_5) LOSSY OBJECT IN PAYLOAD FAIRING

The quality factor measured in a well-stirred reverberation chamber should not change with antenna placement. The two-antenna quality factor measurements were therefore repeated with one antenna raised by placing it on a cardboard, as shown in figure 61. The cardboard was expected to have minimum impact on the Q. The measured energy decay and linear fits are shown in figure 62. The decay is much sharper than that measured with the empty fairing. (Note the change in the horizontal scale relative to figure 60). The corresponding quality factors are compared with those measured in the empty fairing in Table 10. The Q is reduced by 5 dB at 1 GHz and 11 dB at 6 GHz.

Additional investigation shows that the cardboard contained moisture. Liquid water is a strong absorber of microwave energy [23]. Support within the fairing should be styrofoam to avoid loading the cavity.



Figure 61: Cardboard Used as Support to Place a Horn Antenna in Top Cavity of the Fairing

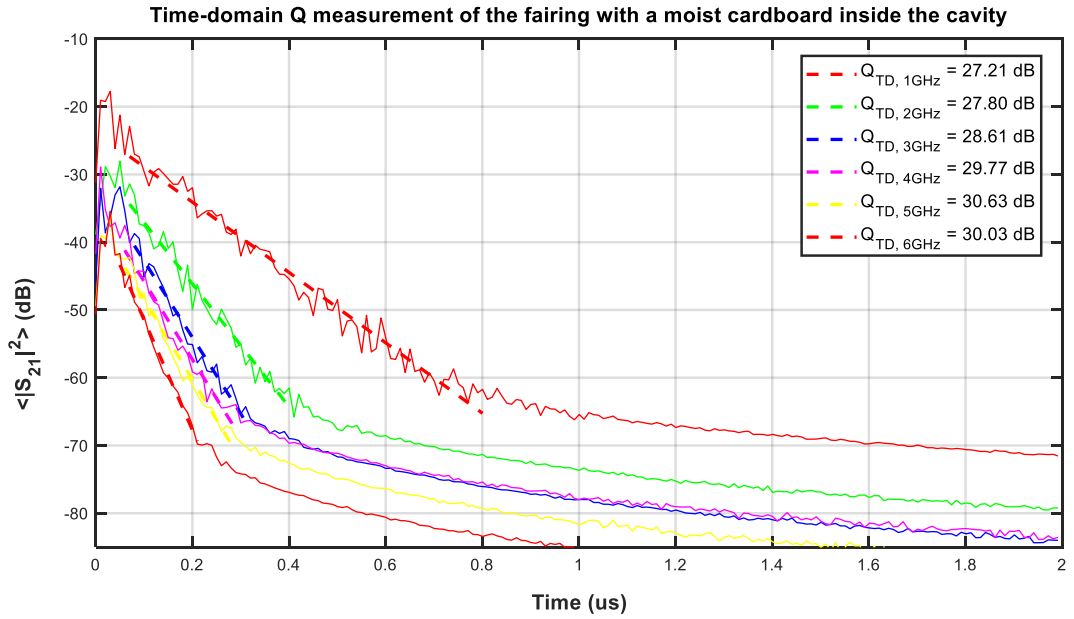


Figure 62: QTD of the Payload Fairing with the Moist Cardboard in the Fairing Cavity

The fairing with cardboard box test setup was also measured in frequency-domain to determine the quality factor of the cavity. The match between the two methods is within the range observed in previous measurements conducted with two horn antennas, shown in figure 63.

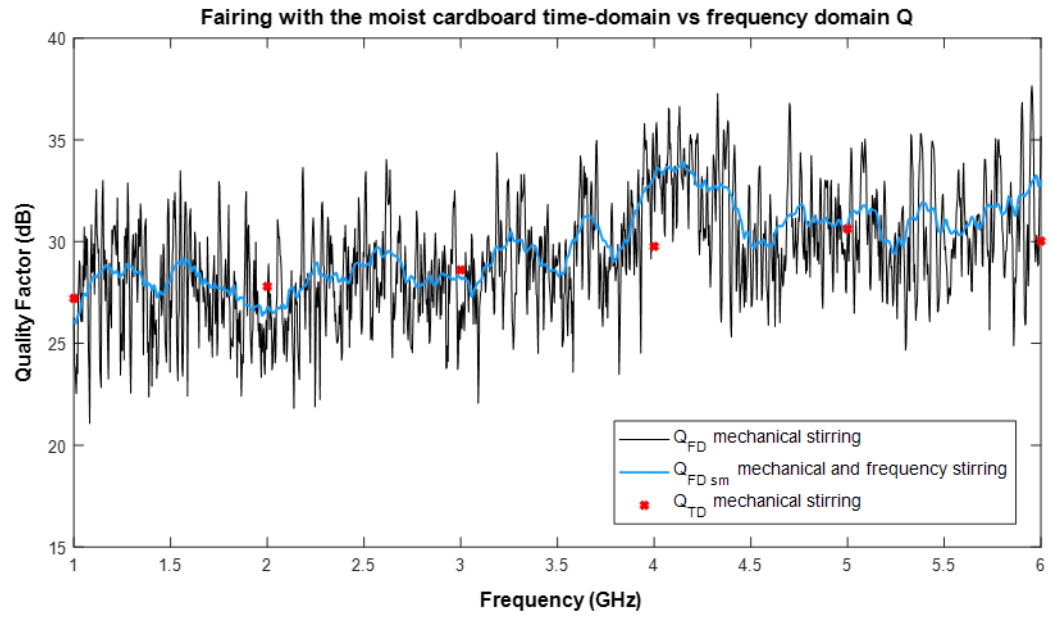


Figure 63: Fairing Single Antenna Q in Frequency and Time Domains

5_6) SPACECRAFT MODEL WITHIN THE FAIRING

The payload surrogate model and payload adapter were then added to the fairing and the two-antenna quality factor measurements repeated. The dual-ridge horn antennas were placed on the fairing base in the same position that was used in empty-fairings measurements, as shown in figure 64.

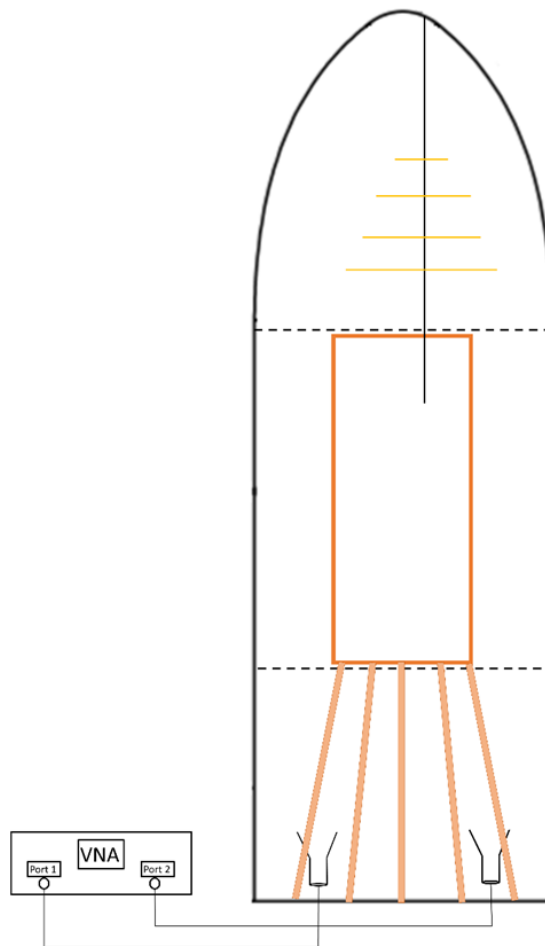


Figure 64: Payload Model Placed Within the Fairing Cavity

The Q was first measured in the frequency domain with averaging over 100 unique tuner positions. Figure 65 compares the measured quality factor when the payload model is placed within the fairing cavity with that measured for the empty fairing.

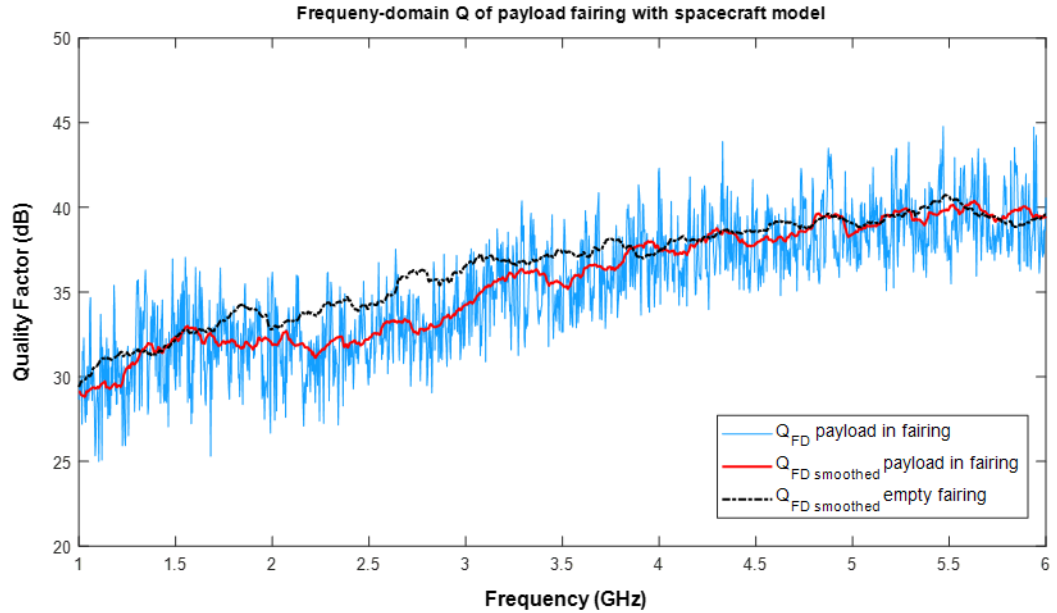


Figure 65: Q of the Fairing with the Payload

Addition of the payload gives a small reduction of the Q from 1.5 GHz to 3.7 GHz but has little effect at other frequencies. The small change in Q by the placement of the cylindrical aluminum payload can be explained from reverberation chamber theory. The quality factor of an ideally closed cavity is [5]

$$Q = \frac{3V\sqrt{2\pi f\mu\sigma}}{4\mu_r A} \quad (5.5)$$

where V is the cavity volume, f is operating frequency, μ is magnetic permeability of the cavity dielectric filling, σ is surface conductivity of the cavity wall, μ_r is relative magnetic permeability, and A is the surface area of cavity.

Equation 5.5 gives the theoretical value of reverberation chamber Q considering only wall-conductivity losses. The aluminum payload model is more conductive than the Cu-Ni fabric in the fairing walls and has considerably less surface area. Moreover, the dominant loss mechanism in the fairing is likely leakage through the flange joints and the tuner-shaft aperture. The primary factor affecting the Q is therefore the reduction in volume of the cavity V . The volume loss due to the payload is 0.12 m^3 of the 1.2 m^3 volume of the empty fairing, or 10%. This corresponds to a 0.45 dB reduction, which is consistent with measured Q reductions. The entire volume of the fairing still behaves as a single cavity despite the addition of the payload.

5_7) FIELD PROBE MEASUREMENT OF Q

Measurements are now performed using the 5 and 10 cm dipole field probes described in Chapter 4. As noted, the field probes must be used at measurement locations other than the base of the fairing due to large volume of the horn antennas. The reflection (or S_{11}) from the probe feeds is first measured in the anechoic and reverberation chambers. The probes were fed through a large aluminum ground plane to mimic their mounting in the fairing. The 5 cm dipole reflection is shown in figure 66. The reverberation chamber measurements were averaged over 100 tuner positions. Excellent agreement between the anechoic and reverberation chamber reflection coefficients was achieved.

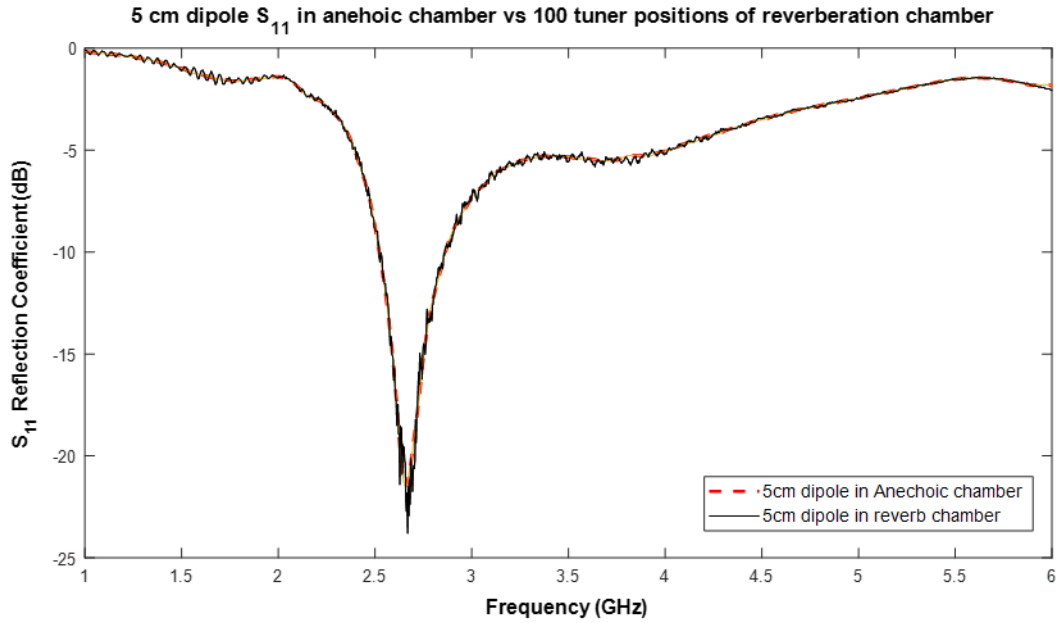


Figure 66: Reflection Coefficient of 5 cm Dipole Probe in Reverberation and Anechoic Chambers

Figure 66 shows a limitation of using a resonant dipole structure to measure the fields within the fairing. Dipoles are highly resonant, as reflected by the deep null in reflection at 2.7 GHz where the dipole is 0.45 wavelengths in length. This leads to high reflections away from the resonances, with the worst case at 1 GHz. Measurement tolerances limit the relative accuracy of measurement losses of this small magnitude, which can greatly affect the correction factor used in equation (5.5). The 5 cm probe therefore cannot be used at the lowest frequencies.

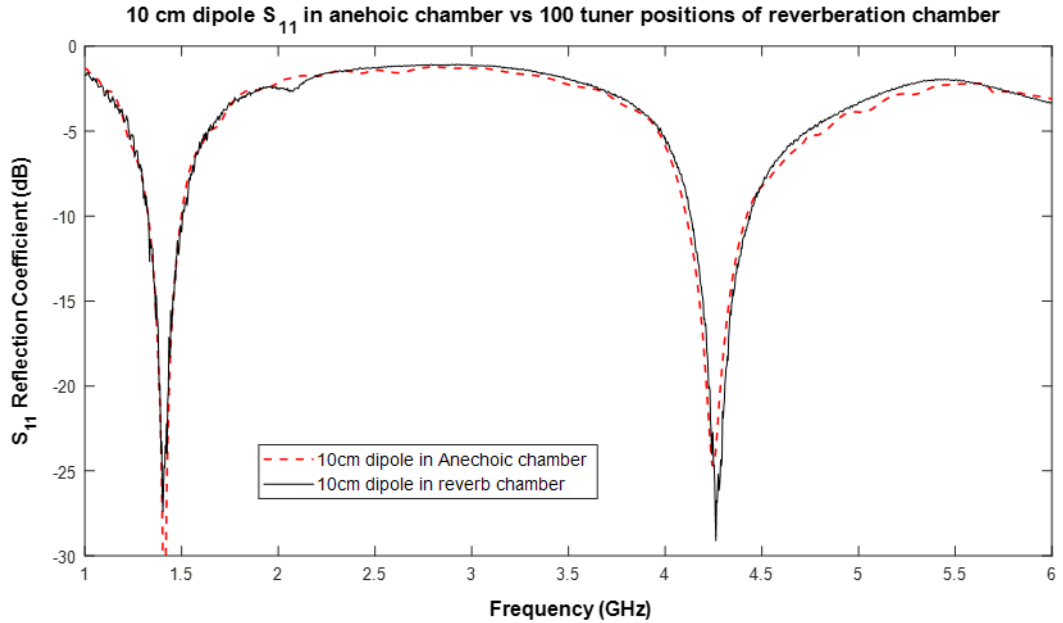


Figure 67: Reflection Coefficient of 10 cm Dipole Probe in Reverberation and Anechoic Chambers

The measured reflections from the 10 cm dipole probe are shown in figure 67. The 10 cm dipole is better matched than the 5 cm dipole below 1.5 GHz, giving a lower reflection. The 10 cm dipole also performs better at the higher frequency limit of 6 GHz. The 10 cm dipole probe is therefore recommended for testing of the power balance model in the model fairing.

Figure 68 shows the 10 cm dipole-probe Q measurements of the fairing local regions with payload in place. Also shown is the Q measured by the horn antennas placed in the bottom cavity. The absorbers are not added for this measurement. All three fairing regions yield similar measured Q levels, again demonstrating that the entire volume within the fairing acts as a single cavity when no absorber is added. The Qs measured with the field probes give a reasonable match with that measured by the horn antennas in the bottom cavity. This demonstrates that the dipole probes are effective in measuring the fields within the fairing. These measurements are used as benchmark for local cavity Q measurements after adding the absorbers.

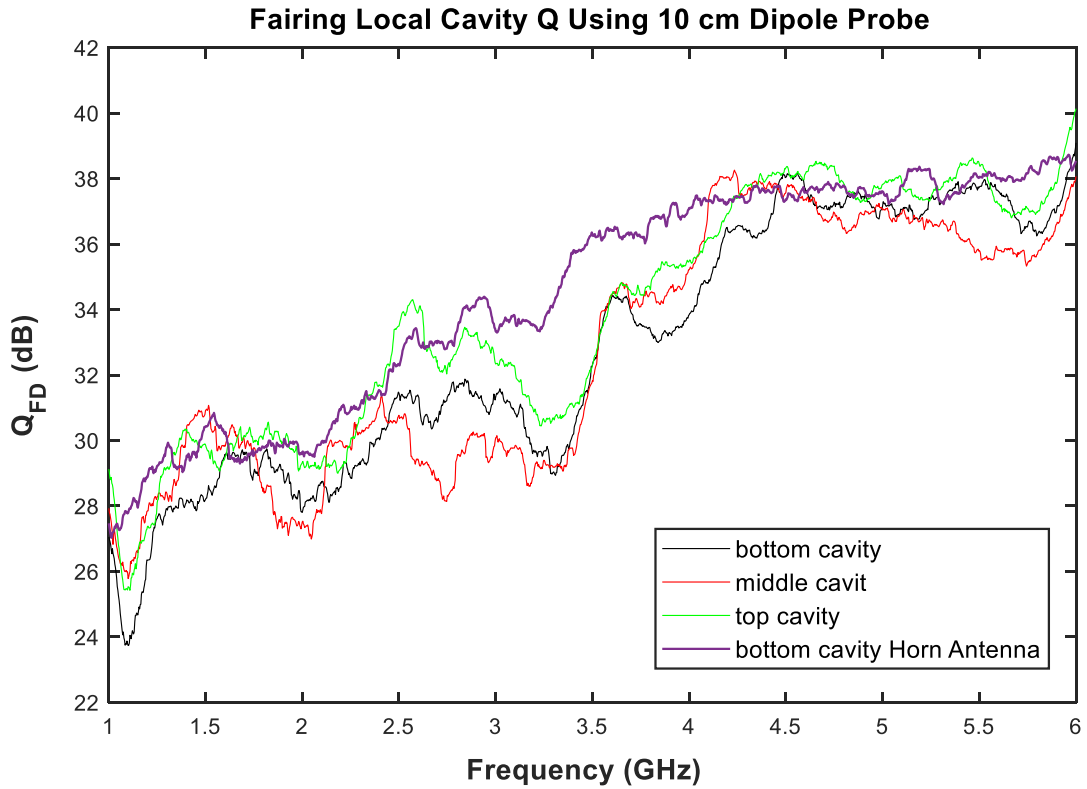


Figure 68: Fairing Local Cavity Q with Payload

5_8) FAIRING LOCAL CAVITY Q WITH ABSORBERS

It was shown earlier that the placement of the spacecraft or payload model within the fairing cavity does not change the quality factor of the cavity significantly. However, the acoustic and RF absorbers add losses and will reduce the Q similar to the reduction when the damp cardboard box was added.

Figure 69 shows the installation of acoustic absorber and RF absorber foams in the region of the fairing where the spacecraft model is placed. The acoustic foam (white) was placed directly on the

fairing wall and the foam RF absorber (black) was placed on that. In figure 69, the lower segment of the acoustic foam is intentionally left exposed to illustrate the installation order of the foams. In final setup shown in the next figure, the acoustic foam is completely covered with the RF foam.



Figure 69: Acoustic Absorbing Foam and RF Absorbing Foam Installed in the Middle Cavity of the Fairing

Figure 70 shows the test configuration of the fairing and payload with absorbers added. The payload is wrapped in sheet RF absorber (gray), modeling the electromagnetic shielding layer that is sometimes placed around payloads during launch. The top and bottom faces of the cylindrical structure of the payload are not covered. Addition of absorber only to the payload region is consistent with actual launch configurations.



Figure 70: Final Assembly of the Absorbing Foams Installed on the Fairing and Payload

Figure 71 shown the quality factor measured in the frequency domain when both measurement probes were placed in the lower fairing region, below the payload. The Q is greatly reduced from that measured when the absorber was not installed in figure 68. In the test setup for local cavity Q measurements, acoustic absorbing and the two RF absorbing materials are present in the fairing cavity, introducing significant losses, lowering the Q of the fairing.

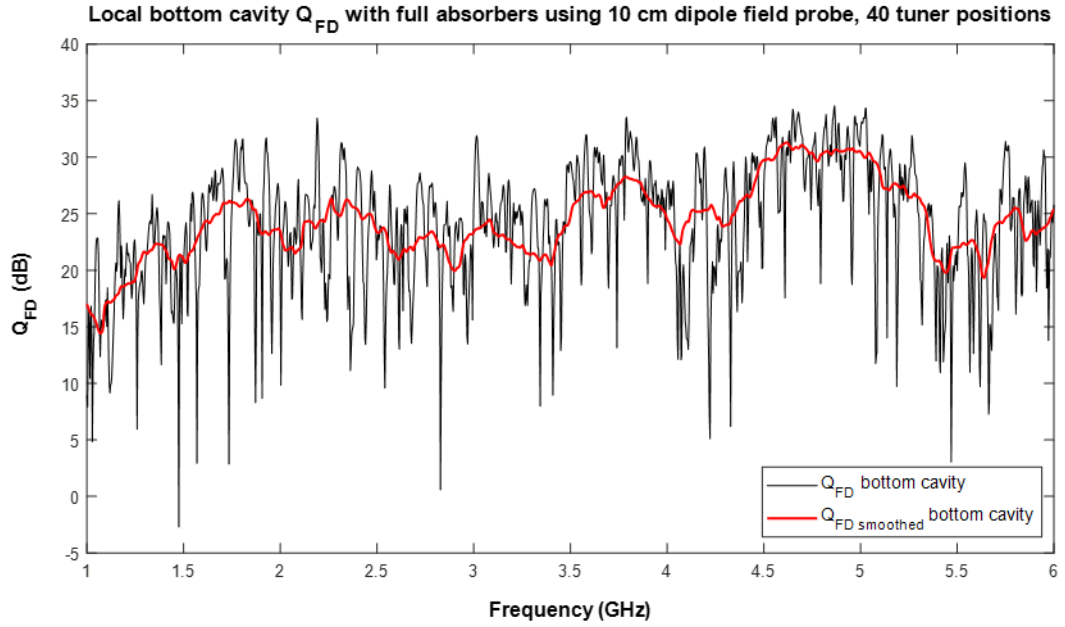


Figure 71: Local Bottom Cavity of the Payload Fairing

The measured quality factors when the measurement probes are placed in the payload region with the absorber in place are shown in figure 72. The measured quality factor is much lower in this case. At 1 GHz, the Q measured in the middle cavity is less than 1 dB (0.93 dB) but it rises to 20 dB at 6 GHz.

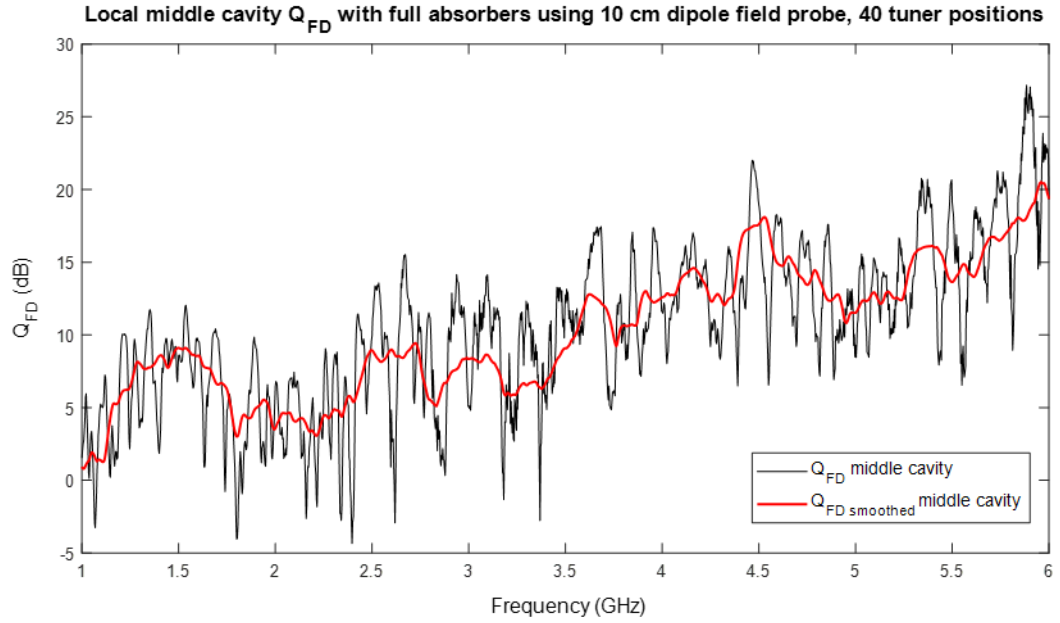


Figure 72: Local Middle Cavity of the Payload Fairing

Finally, the quality factors measured in the nose section of the fairing are shown in figure 73. They are similar in magnitude to the bottom-region values, although the 10 dB rise in Q across the band is not observed in the top region. The Q relatively stays around 22 dB from 1 GHz to 6 GHz with a plateau around 28 dB from 1.5 GHz to 3.0 GHz.

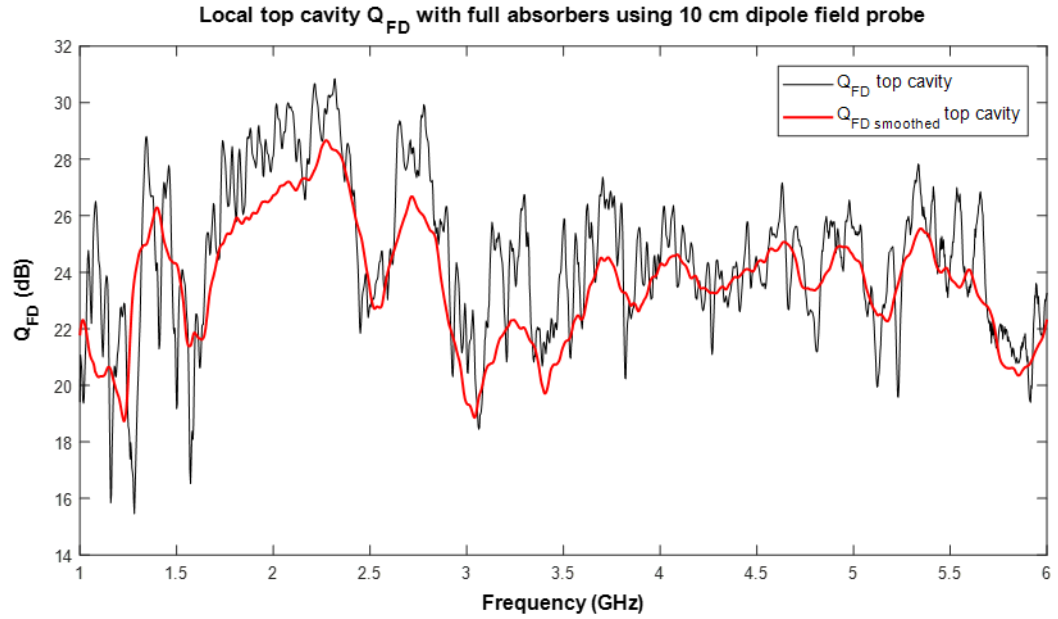


Figure 73: Local Top Cavity of the Payload Fairing

Figure 74 shows the quality factor measurements with absorbers added in one plot for a better observation of the differences between the Q levels at the three measurement points. The considerable disparity in the Q measured in each region indicates that, unlike when no absorber was added, the three regions behave as separate, but coupled cavities. The top and bottom local cavity Qs are reduced from that when no absorber is added (figure 69) due to loss of effective cavity volume as well the leakage of energy into the other regions that is ultimately dissipated in the absorber. The center region Q is determined by the very large direct losses in that sub-cavity. This behavior is consistent with the power-balance model. The results in figure 74 therefore show that this is a good test setup for a subsequent study of power-balance model in the payload fairing.

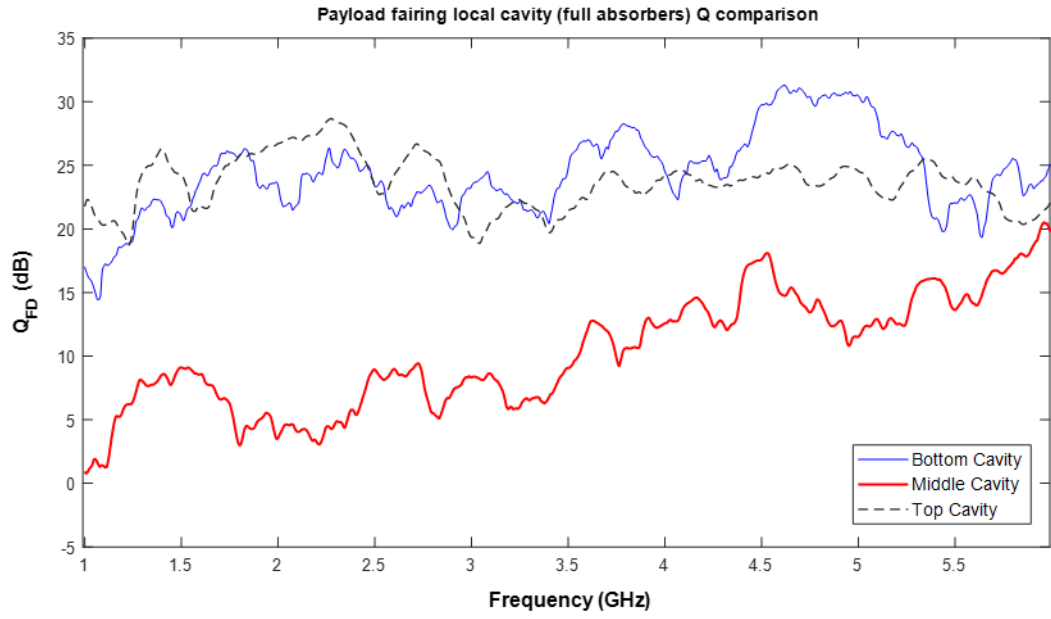


Figure 74: Frequency-Domain Quality Factor for the Three Local Cavities of the Payload Fairing

CHAPTER VI

CONCLUSION

A model composite fairing has been fabricated at the Oklahoma State University to represent the electromagnetic environment within actual payload fairings during launch. The OSU fairing model is fabricated from fiberglass and uses a conductive-fabric layer to provide shielding. A mechanical tuner is placed at the nose of the fairing to randomize the electromagnetic field within the fairing cavity. A removable payload model and a payload adapter model are included in the fairing. The electromagnetic fields in payload fairing can be represented by the statistical theory of reverberation chamber where characteristics of the field such as amplitude, phase and polarization become random variable.

The composite payload fairing model is 2.44 m high with 0.8 m radius at its cylindrical section. The fairing has a total volume of 1.212 m^3 and total surface area of 7.38 m^2 . The cylindrical section of the fairing uses a layer of vinyl foam in addition to fiberglass layers for structural rigidity. Preliminary studies of the microwave reflectivity of the Cu-Ni fabric and its performance when used to create a small avionics size validated its use as the shielding layer in the fairing model.

The fiberglass and Cu-Ni fabric structure gave a robust and lightweight model that could be easily be positioned for measurements. The payload was represented by a cylindrical aluminum structure and supported by a truss-like structure which served as the payload adapter of the fairing. An

electromagnetic shielding gasket was used at the fairing flanges to minimize energy leakage. A mechanical, z-fold conductive tuner was placed slightly off-center in the nose section that could be rotated to provide random realizations of the electromagnetic field within the fairing. A field probe consisting of a 10 cm dipole mounted on a 10 cm rigid coaxial line was designed and fabricated to perform field measurements at arbitrary points within the fairing. The performance of the field probe was validated through comparison of cavity quality factors measured with both the field probes and well-matched dual ridge horn antennas.

The quality factor the payload fairing cavity was measured using time-domain and frequency domain approaches. The measurements were performed both the when the fairing was empty and various combinations of the payload model and RF and acoustic absorbers were added. The quality factor of the empty fairing ranged from about 32 dB at 1 GHz to 41 dB at 6 GHz. These Qs are considerably below that expected from the conductive losses of the shielding material, indicating that there was significant leakage out of the cavity despite the use of the shielding gaskets. However, the cavity did behave similarly to an over-moded reverberation chamber when both mechanical and frequency stirring were combined. The quality factor measured in the time-domain was always slightly higher than that measured in the time-domain due to the radiation efficiency of the measurement probes.

Measurement in three different regions of the fairing yielded similar quality factors that were only slightly below that for the empty fairing when no absorber was added, indicating that the unfilled fairing volume behaves as a single resonant cavity under these conditions. However, there was major reduction in Q when the absorbers were added to the payload region. The Q measured in the center cavity was substantially lower than that measured in the top and bottom regions, indicating that the absorbers made the three regions behave as separate but coupled cavities. This operation is well suited to analysis by the power-balance model.

REFERENCES

- [1] R. Brewer and D. Trout, "Modern spacecraft - antique specifications," 2006 IEEE International Symposium on Electromagnetic Compatibility, 2006. EMC 2006., Portland, OR, USA, 2006, pp. 213-218.
- [2] D. H. Trout, P. F. Wahid and J. E. Stanley, "Electromagnetic cavity effects from transmitters inside a launch vehicle fairing," 2009 IEEE International Symposium on Electromagnetic Compatibility, Austin, TX, 2009, pp. 70-74.
- [3] David A. Hill, "Aperture Excitation of Electrically Large, Lossy Cavities," in *Electromagnetic Fields in Cavities: Deterministic and Statistical Theories*, IEEE, 2009, pp.151-164
- [4] P. G. Bremner, G. Vazquez, D. H. Trout and P. R. Edwards, "Shielding Effectiveness – When to Stop Blocking and Start Absorbing," 2019 IEEE International Symposium on Electromagnetic Compatibility, Signal & Power Integrity (EMC+SIPI), New Orleans, LA, USA, 2019, pp. 284-291.
- [5] D. A. Hill, *Electromagnetic Fields in Cavities: Deterministic and Statistical Theories*, New Jersey: John Wiley & Sons, 2009, pp. 91-148.
- [6] C. A. Balanis, *Advanced Engineering Electromagnetics*, 2nd ed. Hoboken, NJ: John Wiley & Sons, 2012.

- [7] D. M. Pozar, *Microwave Engineering*, 4th ed. Hoboken, NJ: John Wiley & Sons, 2012.
- [8] R. E. Richardson, "Reverberant microwave propagation," Naval Surface Warfare Center - Dahlgren Division, Virginia, 22448-5100, Tech.Rep. NSWCDD/TR-08/127, 2008.
- [9] D. A. Hill, "Plane wave integral representation for field in reverberation chambers," *IEEE Trans. Electromagn. Compat.*, vol. 40, no. 3, pp. 209-217, Aug. 1998.
- [10] David A. Hill, "Aperture Excitation of Electrically Large, Lossy Cavities," in *Electromagnetic Fields in Cavities: Deterministic and Statistical Theories*, IEEE, 2009, pp.151-164
- [11] J. C. West, V. Rajamani and C. F. Bunting, "Frequency- and time-domain measurement of reverberation chamber Q: An in-silico analysis," 2016 IEEE International Symposium on Electromagnetic Compatibility (EMC), Ottawa, ON, 2016, pp. 7-12.
- [12] J. C. West, J. N. Dixon, N. Nourshamsi, D. K. Das and C. F. Bunting, "Best Practices in Measuring the Quality Factor of a Reverberation Chamber," in *IEEE Transactions on Electromagnetic Compatibility*, vol. 60, no. 3, pp. 564-571, June 2018.
- [13] N. Nourshamsi, J. C. West and C. F. Bunting, "Required bandwidth for time-domain measurement of the quality factor of reverberation chambers," 2017 IEEE International Symposium on Electromagnetic Compatibility & Signal/Power Integrity (EMCSI), Washington, DC, 2017, pp. 481-485, doi: 10.1109/ISEMC.2017.8077918.
- [14] B. F. Kutter et al., "Ongoing launch vehicle innovation at United Launch Alliance," 2010 IEEE Aerospace Conference, Big Sky, MT, 2010, pp. 1-14, doi: 10.1109/AERO.2010.5446742.
- [15] W. Hughes, A. McNelis, M. McNelis, "Acoustic Test Characterization of Melamine Foam for Usage in NASA's Payload Fairing Acoustic Attenuation Systems," NASA/TP – 2014-218127.

- [16] M. Hallett, J. Redell, "Technique for Predicting the RF Field Strength Inside an Enclosure," NASA/TP - 1998-206864, 1998.
- [17] Reverb.okstate.edu, "Oklahoma State University Robust Electromagnetic Field Testing and Simulation Laboratory", 2020. [Online]. Available: <https://reverb.okstate.edu/>. [Accessed: 10-Feb-2020].
- [18] Ets-lindgren.com, "SMART 80 Reverb Chambers", 2019. [Online]. Available: <http://www.ets-lindgren.com/products/chambers/emc-chambers/smart%E2%84%A2-reverb-chambers/5007/500703>. [Accessed: 17-Mar-2020].
- [19] D. H. Trout, "Electromagnetic Environment in Payload Fairing Cavities," Dissertation, University of Central Florida, 2012.
- [20] C. Holloway, H. Shah, R. Pirkl, W. Young, D. Hill, J. Ladbury, "Reverberation Chamber Techniques for Determining the Radiation and Total Efficiency of Antennas," IEEE Trans. Electromagn. Compat., vol. 60, no. 4, pp. 1758-1770, Apr. 2012.
- [21] D. Green, V. Rajamani, C. Bunting, B. Archambeault, S. Connor, "One-Port Time Domain Measurement Technique for Quality Factor Estimation of Loaded and Unloaded Cavities," 2013 IEEE International Symposium on Electromagnetic Compatibility.
- [22] V. Rajamani, C. Bunting, J. West, "Differences in Quality Factor Estimation in Frequency and Time Domain," 2012 Asia-Pacific Symposium on Electromagnetic Compatibility.
- [23] L. A. Filins'kyy, "Absorbed media dielectric permittivity research in form of water foam specimens," 2005 5th International Conference on Antenna Theory and Techniques, Kyiv, Ukraine, 2005, pp. 515-517, doi: 10.1109/ICATT.2005.1497038.

APPENDICES

APPENDIX A: CODE FOR TIME-DOMAIN Q MEASUREMENT

```
filename = 'test_072_RC.xlsx';

% Reading S21 amplitude and phase from VNA data
S21Amp = xlsread(filename, 'S21 Amplitude');
S21Phase = xlsread(filename, 'S21 Phase');

S21Amp_lin = 10.^ ((S21Amp)./20);

% Putting S21 amplitude and phase in complex form to do FFT
S21Comp = S21Amp_lin .* exp(1i*pi*S21Phase/180);

S21Trans = ifft(S21Comp); % MATLAB FFT routine

S21_mag_sq = abs(S21Trans).^2; % |S21|^2

S21_ensem = mean(S21_mag_sq,2); % <|S21|^2>

S21_ensem_dB = 10 * log10(S21_ensem); % dB conversion of
ensemble, mag-squared S21

Bw = 100e6; % bandwidth
l = length(S21Comp); % length of data samples (1601)
Fs = Bw/l; % sampling frequency

% Prepare the horizontal time axis in us and plot <|S21|^2> in dB
Ts = linspace(0, 1/(Fs), l);
plot(Ts, S21_ensem_dB)

% This part is LINE FIT using MATLAB routines
x = Ts(1:800); % define data
y_sub = S21_ensem_dB(1:800);
y = y_sub';

x1 = x(55); % define interval
x2 = x(800);

xrange = x(find(x == x1):find(x == x2)); % pick out x and y
vals in interval
yrange = y(find(x == x1):find(x == x2));
```

```

p = polyfit(xrange, yrange, 1);      % do linear curve fit
yfit = polyval(p, xrange);

figure(2)
hold on; grid; box
plot(x*1e6,y,'k')    % this is the same plot as above but with
less data samples
plot(xrange*1e6,yfit,'r','linewidth',1.5)    % plots the line fit

xlabel('Time (us)')
ylabel('<|S_{21}|^2> (dB)')

% Quality factor calculation (Q = 2*pi * f * tau_rc)
m = abs(p(1))    % slope of linear fit
Fc = 1e9    % Operating frequency

Q = 2*pi * Fc * (4.3429/m);    % Time-domain (Q) factor
Q_dB = 10 * log10(Q)

```

APPENDIX B: CODE FOR FREQUENCY-DOMAIN Q MEASUREMENT

```

close all; clear all; clc
filename = 'test_070_RC.xlsx';

S21Amp = xlsread(filename,'S21 Amplitude');
S21Phase = xlsread(filename,'S21 Phase');
S11Amp = xlsread(filename,'S11 Amplitude');
S11Phase = xlsread(filename,'S11 Phase');
S22Amp = xlsread(filename,'S22 Amplitude');
S22Phase = xlsread(filename,'S22 Phase');

S21Amp_lin = 10.^ ((S21Amp)./20);
S11Amp_lin = 10.^ ((S11Amp)./20);
S22Amp_lin = 10.^ ((S22Amp)./20);

S21_Comp = S21Amp_lin .* exp(1i*S21Phase*pi/180);
S11_Comp = S11Amp_lin .* exp(1i*S11Phase*pi/180);
S22_Comp = S22Amp_lin .* exp(1i*S22Phase*pi/180);

S21_mag_sq = abs(S21_Comp) .^ 2;

S21_ensem = mean(S21_mag_sq, 2);

S11_ensem = mean(S11_Comp, 2);
S22_ensem = mean(S22_Comp, 2);

S11_mag = abs(S11_ensem);

```

```

S22_mag = abs(S22_ensem);

eta_1 = 1 - S11_mag .^ 2;
eta_2 = 1 - S22_mag .^ 2;

f = linspace(1e9,6e9,1601)';
lambda = (3e8 ./ f);
lambda_cube = lambda .^3;
V = 401;      % SMART 80 volume in m^3

% WITHOUT SMOOTHING
Q_fd = (16 * pi^2 * V) ./ (lambda_cube) .* S21_ensem;
Q_fd_cor = (Q_fd) ./ (eta_1 .* eta_2);
Q_fd_cor_dB = 10 * log10(Q_fd_cor);

figure(1)
plot(f/1e9, Q_fd_cor_dB)
hold on
xlabel('Frequency (GHz)')
ylabel('Q_{FD} (dB)')
legend('Q_{FD}', 'Q_{TD, old}', 'Q_{TD, new}')
%title('Reverberation Chamber Quality Factor Measurement Using
Dual-Ridged Horn Antennas')
%ylim([30 60])

% Q_TD data points
x_TD = [1 2 3 4 5 6];
y_TD = [42.36 44.77 46.02 46.71 47.34 47.78];
scatter(x_TD, y_TD, 'rx', 'linewidth',2)
y_TD_n = [45.37 47.78 49.03 49.72 50.35 50.79];
scatter(x_TD, y_TD_n, 'bx', 'linewidth',2)

```

VITA

Shabir Ahmad Kabiri

Candidate for the Degree of

Master of Science

Thesis: REVERBERANT ELECTROMAGNETIC FIELDS WITHIN LAUNCH
VEHICLE PAYLOAD FAIRINGS

Major Field: Electrical Engineering

Biographical:

Education:

Completed the requirements for the Master of Science in Electrical Engineering at Oklahoma State University, Stillwater, Oklahoma in July 2020.

Completed the requirements for the Bachelor of Science in Electrical Engineering at the United State Military Academy, West Point, New York in 2016.

Experience:

Graduate Research Assistant under Dr. Jim West, Oklahoma State University, Stillwater, OK (Feb 2019 - May 2020)

Radio Frequency Engineer at Afghan Wireless Communication, Kabul, Afghanistan (2016 - 2018)

Undergraduate research assistant, North Carolina State University, Raleigh, NC (July 2015 - Aug 2015)